**PATZ1 Reinstates a Growth-Permissive Chromatin Landscape in Adult Corticospinal Neurons After Injury**

Anisha S. Menon[1,2], Manojkumar Kumaran[1,3], Deepta Susan Beji[1,3], Dhruva Kumar Kesireddy[1,3], Netra Krishna[1], Shringika Soni[1], Yogesh Sahu[1,2], Sneha Manjunath[1], Katha Sanyal[1], Meghana Konda[1] and Ishwariya Venkatesh[1*]

[1]Council of Scientific and Industrial Research (CSIR) – Centre for Cellular and Molecular Biology (CCMB), Hyderabad 500007, Telangana, India

[2] Academy of Scientific and Innovative Research (AcSIR), Ghaziabad 201002, Uttar Pradesh, India

* To whom correspondence should be addressed. Email: ishwariya@ccmb.res.in

[3]Manojkumar Kumaran, Deepta Susan Beji, Dhruvakumar Kesireddy contributed equally to this work

**Summary**

Axon regeneration fails in the adult central nervous system in part because chromatin at growth-associated loci becomes progressively inaccessible during maturation. Using bulk and single-nucleus ATAC-seq across developmental timepoints, we identified two postnatal waves of chromatin closure at growth-gene promoters and enhancers, coinciding with withdrawal of GC-stripe transcription factors. Comparing intracortical and thoracic spinal cord injuries, we found that lesion proximity to the soma determines the extent of chromatin reopening, with proximal injury reactivating an order of magnitude more regulatory elements. The stripe factor PATZ1 emerged as a molecular correlate of this distance effect. AAV-mediated PATZ1 delivery after distal injury reopened thousands of growth enhancers, deposited H3K27ac marks, and reorganised three-dimensional genome architecture, as revealed by CUT&RUN and Hi-C. Integrated single-nucleus RNA-seq showed that chromatin opening alone produces modest transcriptional changes, indicating that additional pro-growth factors are required. These findings establish epigenetic priming as a targetable prerequisite for CNS repair.

**Key words**

**Epigenetics, Neuronal regeneration, Chromatin remodelling, Transcriptional regulation, Genome architecture, PATZ1, Spinal Cord Injury, Enhancers, H3K27Ac marks, CTCF boundaries**

## Introduction

The adult central nervous system (CNS) is largely incapable of self-repair, leaving traumatic brain and spinal injuries, as well as many neurodegenerative disorders, with few restorative options [1–3]. This regenerative failure reflects not only an inhibitory extracellular milieu but also intrinsic brakes that tighten as neurons mature [1,2,4–12]. One of the most stringent intrinsic barriers is a progressive closure of chromatin around growth-associated loci, which sequesters regenerative programmes from the transcriptional machinery [13,14]. Broad histone-deacetylase inhibitors offer only limited benefit, presumably because they act indiscriminately on the neuronal epigenome [14]. A precise means of re-opening chromatin specifically at pro-growth regions, therefore, remains a major unmet need.

Although decades of work have illuminated transcription-factor networks that promote CNS outgrowth [4,5,8,7,15–27],more recent studies point to epigenetic control as an additional, decisive layer [28–35]. In zebrafish retinal ganglion cells and in mammalian peripheral neurons, axotomy triggers selective chromatin relaxation that permits binding of growth-inducing factors [19,22,31,36,37]. By contrast, central axons show little or no such epigenomic response, and disrupting chromatin architecture in otherwise regeneration-competent neurons blocks repair [36,37].Yet we still lack a developmental map of chromatin closure in CNS projection neurons, an understanding of whether injury distance influences their epigenetic plasticity, and a strategy to target chromatin opening without broad collateral effects.

Here, we chart chromatin accessibility in mouse corticospinal neurons from embryogenesis through adulthood and after spinal cord injury. We find that growth-gene loci close in two discrete post-natal waves (P0–P4 and P7–adult) and that injury delivered near the soma elicits a ten-fold stronger chromatin response than an equivalent lesion in the thoracic cord. Motif and footprint analyses identify the GC-binding zinc-finger protein PATZ1 as abundant during the growth-competent period, lost in adults, and selectively redeployed by proximal injury. Viral delivery of PATZ1 to adult cortex after thoracic crush re-opens thousands of enhancers, installs H3K27ac at growth genes and reshapes 3-D genome architecture, thereby converting a muted distal-injury response into a developmental-like growth state. These findings position PATZ1 as a tractable lever for targeted chromatin remodelling and suggest that pairing stripe-factor delivery with existing pro-regenerative cues could advance functional repair of the adult CNS.

## Results

### Two discrete postnatal contractions of chromatin accessibility at axon-growth genes

We first asked when forebrain neurons surrender the open chromatin landscape that supports developmental elongation. Public ENCODE bulk ATAC-seq datasets span embryonic day 11 (E11) to birth but are sparse thereafter. We performed additional bulk ATAC-seq on forebrain tissue at P0, P4, P7, and adult timepoints to extend the developmental series (Supplementary Figure S2-A; Supplementary Table S2). Both ENCODE and in-house datasets were generated from forebrain tissue. To enable comparison between datasets, we applied batch correction using a negative binomial regression framework, with successful correction confirmed by PCA (Supplementary Figure S1-A; Supplementary Table S1; see Methods for details). Because ENCODE and in-house data were generated under different conditions, we present them in separate panels and interpret them as complementary rather than directly comparable (Figure 1A-B). We acknowledge that bulk ATAC-seq on heterogeneous forebrain tissue captures accessibility across multiple cell types, and that cell-type-specific changes may be diluted or masked by other populations. However, bulk accessibility profiles can still reveal broad developmental trends in chromatin architecture, and harnessing publicly available ENCODE data allowed us to maximise temporal coverage without duplicating existing resources.

To examine chromatin dynamics at genes relevant to axon growth, we employed two complementary approaches. First, we curated 291 promoters and 1,228 enhancers flanking genes implicated in axon guidance, cytoskeleton dynamics, cell-growth regulation, chromatin remodelling, DNA-damage repair, and nervous-system development (Figure 1C-D; Supplementary Table S1). We selected these categories because axon guidance and cytoskeleton genes directly mediate growth cone navigation and extension; cell-growth regulators control the metabolic and signalling programmes required for elongation; chromatin remodellers may enable or constrain access to growth programmes; DNA-damage repair genes were included because they are upregulated upon treatment with pro-regenerative transcription factors such as KLF6 and Nr5a2, and because highly interacting chromatin regions, including enhancers and super-enhancers that form long-range loops, are enriched in DNA repair factors, suggesting that protection from double-strand breaks at these sites is essential during active transcription [38]; and nervous-system development genes encompass broad neurodevelopmental programmes.

Accessibility at these growth-gene promoters was not static. In early embryos (E11-E12), the vast majority of loci were only modestly accessible. Accessibility then rose monotonically, peaking between E18 and P0 in concert with the period of brisk CST outgrowth (Figure 1C; Supplementary Table S1). Instead of plateauing, accessibility fell during postnatal ages. Quantitative modelling revealed two kinetically distinct contractions: a first wave between P0 and P4 that imposed mild-to-moderate restriction (20-50% loss of signal at 43% of promoters [125 of 291] and 48% of enhancers [589 of 1,228]), and a second wave between P7 and adulthood that produced more extensive closure, with at least 70% loss at 51% of promoters (148 of 291) and 56% of enhancers (688 of 1,228). By maturity, 95% of promoters (approximately 275) and 87% of linked enhancers (approximately 1,067) had lost at least half of their peak accessibility, leaving only a residual subset (5% of promoters [approximately 16] and 13% of enhancers [approximately 161]) partly open (Supplementary Figure S2-B-E; Supplementary Table S2).

We note that the P7-to-adult interval spans several weeks and likely encompasses gradual changes rather than a discrete transition; the exact timing of closure within this window remains undefined by our sampling. We therefore interpret P4 and P7 as informative boundaries rather than as precise developmental checkpoints. By P4, many growth loci have begun to restrict, and by P7, the majority show substantial closure, though residual accessibility persists into adulthood at some sites.

When we clustered accessibility trajectories, promoters behaved largely synchronously, whereas enhancers displayed pathway-specific variation. Between P0 and P4, 70.7% of promoters showed restriction compared to 69.1% of enhancers; by the P7 to adult transition, 64.3% of promoters and 58.0% of enhancers were restricted (Figure 1E-F; Supplementary Table S1). Despite this broad closure, enhancers for nervous-system-development genes retained measurable openness into adulthood, with roughly one-quarter remaining above the 50% accessibility threshold, suggesting a need for ongoing plasticity in that pathway. Enhancers governing DNA-repair genes were even more refractory: nearly 30% retained embryonic-level accessibility in the adult. Beyond potentially supporting rapid lesion-induced repair, this persistent openness may preserve architectural flexibility required for long-range enhancer-promoter contacts that activate genome-maintenance pathways, though this hypothesis requires direct testing (Figure 1C-D; Supplementary Table S1).

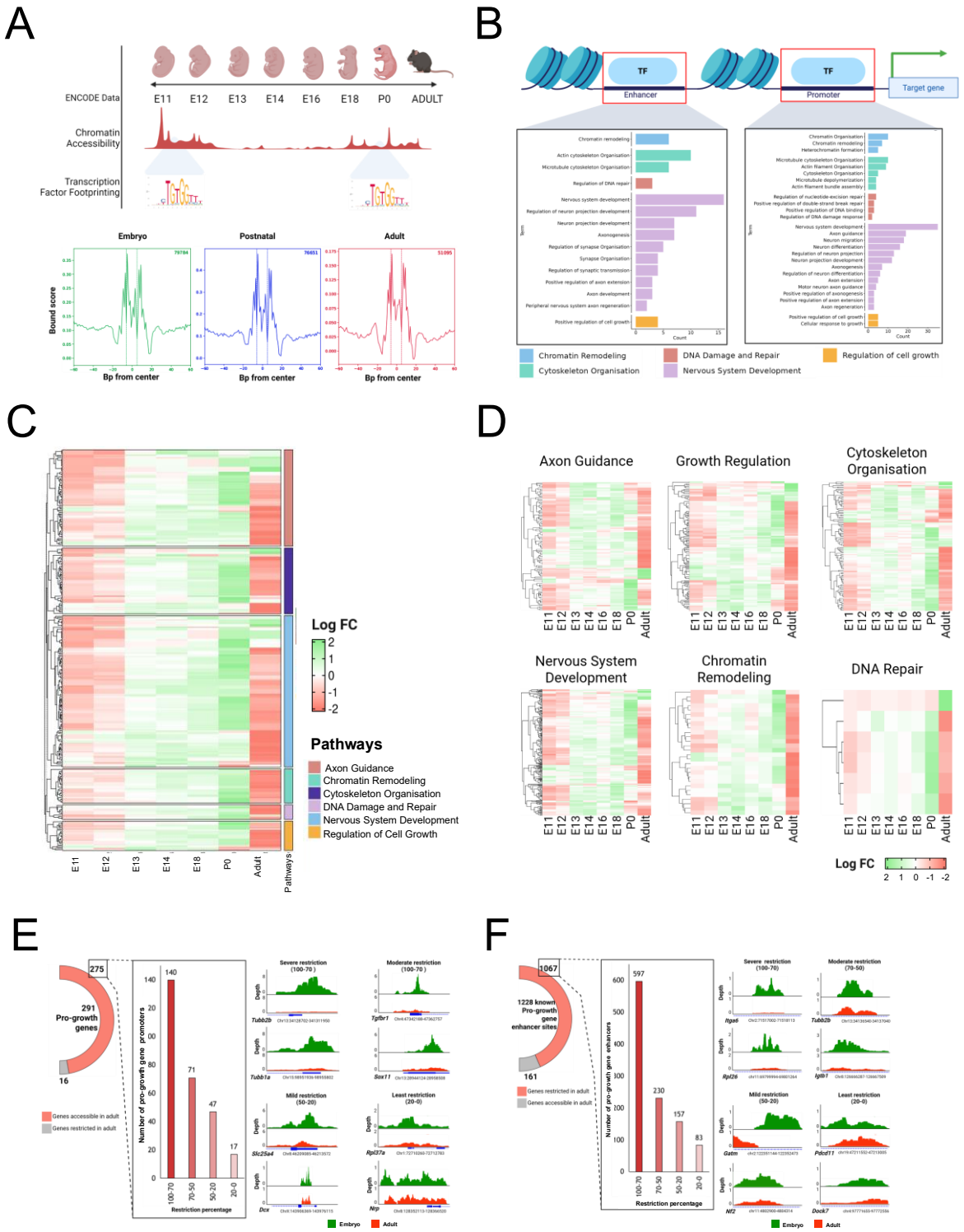


**Figure 1. ATAC-seq reveals severe restriction of promoter and enhancer accessibility in pro-growth genes across age.** (A) Top panel: Schematic diagram of ENCODE ATAC-seq datasets isolated from the motor cortex of mice from early embryonic ages, Postnatal Day 0 (P0), and adult mouse cortex were analysed for genome-wide patterns in chromatin accessibility. Bottom panel: Representative traces of transcription factor footprinting across

age. (B) Pro-growth gene-specific promoters and enhancers were isolated for further analysis based on Gene Ontology (GO) Analysis. (p-value <0.05). (C) Heatmap of promoter accessibility across ages, showing high accessibility at P0 (green) neurons and reduced accessibility in adults (red) (p-value <0.05). (D) Heatmap of enhancer accessibility across age for growth-related GO terms (p-value <0.05). (E) UCSC genome browser examples of pro-growth gene promoters with varying degrees of restriction in adults (275 total; >50% show significant restriction). (F) UCSC genome browser examples of enhancer regions with varying levels of restriction in adults (1,067 total; most show >50% restriction).

TF-footprinting across the same series exposed changes in binding landscapes. The embryonic and early-postnatal period was dominated by orphan nuclear receptors (NR2C1/2, NR2F1/6) and RAR-related factors that coordinate early development (Supplementary Figure S2-F left; Supplementary Table S2). Between P4 and P7, these footprints diminished, replaced by strong occupancy of SP1, SP2, and MAZ (Supplementary Figure S2-F middle; Supplementary Table S2). By adulthood, JUN, JUNB, and MEF2A became the prevailing binders (Supplementary Figure S2-F right; Supplementary Table S2). The timing of these TF exchanges correlates with the two waves of chromatin contraction, which hints at active regulation of promoter-enhancer closure.

Second, to comprehensively profile chromatin accessibility without bias from manual curation, we retrieved complete gene sets associated with GO terms relevant to neuronal growth and plasticity, including axonogenesis, axon guidance, neuron projection guidance, regeneration, central nervous system development, axon extension, actin cytoskeleton organisation, chromatin remodelling, neuron development, RNA polymerase II-dependent transcription, signal transduction, and neurogenesis. Using their GO IDs, we compiled all genes annotated to these categories and generated heatmaps (Supplementary Figure S1-B). The patterns observed from the unbiased GO-based gene sets were consistent with those from the curated list, supporting the robustness of our findings across both analytical frameworks.

**A distal thoracic crush activates a modest, broadly distributed epigenomic response**

Seven days after complete T8 crush, an interval when axonal degeneration has stabilised but spontaneous sprouts are still scarce, we isolated nuclei from motor cortex and generated 3' single-nucleus ATAC-seq (snATAC-seq) libraries (Figure 2A). To identify

corticospinal-enriched populations, we performed anterograde AAV tracing two weeks before injury, injecting AAV-CAG-GFP into layer V motor cortex to label descending projection neurons. We then used fluorescence-activated nuclear sorting (FANS) to enrich for GFP-positive nuclei prior to library preparation (Supplementary Figure S3-A-D). Within the snATAC-seq data, we identified layer 5 extratelencephalic (L5 ET) neurons based on chromatin accessibility at marker genes including *Etv1*, *Crym*, and *Mrpl11* (Figure 2-B, Supplementary Figure S4-E-F). L5 ET neurons include corticospinal neurons but also other subcortical projection neurons; we therefore refer to this population as L5 ET throughout rather than as CST specifically.

After quality control, 3,351 L5 ET nuclei were retained (median of approximately 8,400 unique fragments per cell). snATAC-seq library quality was confirmed by TSS enrichment and fragment size distribution analysis (Supplementary Figure S4-A-B). Figure 2B shows the UMAP embedding of snATAC-seq data with L5 ET clusters highlighted (Supplementary Figure S4-C-D), and Figure 2C displays accessibility at L5 ET marker loci. Comparison with age-matched uninjured cortex uncovered 5,482 regions that increased and 6,000 that decreased in accessibility (Figure 2D; Supplementary Table S3). Enhancers dominated the gains: 74% lay more than 2 kb from an annotated transcription start site.

Accessibility increases were generally modest: 62% of up-peaks fell between log2FC 1.5 and 2.5, and only 3.4% exceeded log2FC 3. Despite this limited amplitude, virtually every functional category in our growth list was represented. Counting differential peaks by pathway (Figure 2E-G) showed regulation of cell growth (402 peaks), cytoskeleton organisation (306), nervous-system development (206), and axon guidance (157) all responding, whereas DNA-damage and repair contributed 43 peaks. Median fold-changes differed across categories: regulation-of-growth and cytoskeleton modules centred on log2FC of approximately 1.9, nervous-system development and chromatin-remodelling on log2FC of approximately 1.4, and axon-guidance loci on log2FC of approximately 1.2.

Bubble-plot clustering of the 5,482 gains emphasised this bias in magnitude rather than in target selection (Figure 2H; Supplementary Table S3). Terms linked to DNA-damage response, cell-cycle control, cytoskeleton regulation, and chromatin remodelling occupied the largest bubbles, but axon-guidance and synaptogenic terms were also present, albeit with smaller effect sizes. Thus, distal spinal injury re-opens regulatory DNA across major growth pathways, yet the depth of opening is low-to-moderate. Previous transcriptomic studies of

distal spinal injury reported only negligible changes in growth-gene expression[6]. In contrast, our data suggest that the chromatin landscape does register the injury, albeit in a muted fashion.

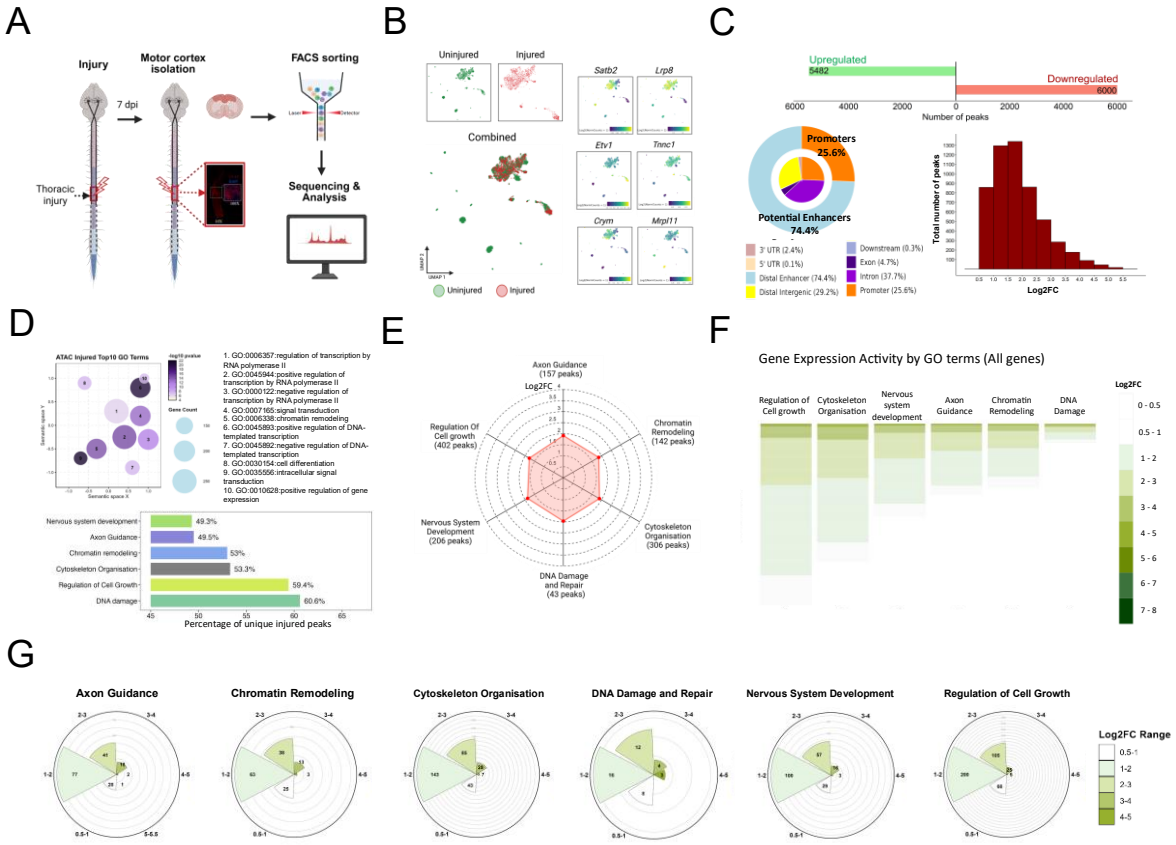


**Figure 2. Single-nuclear (sn)ATAC-seq reveals that CNS neurons mildly open the chromatin post-injury at key loci.** (A) Schematic representation of single-nucleus ATAC-seq (snATAC) experimental workflow. (B) Uniform Manifold Approximation and Projection (UMAP) dimensional reduction plot showing single-nucleus ATAC-seq clustering. The plot displays three conditions: Uninjured (control, green), Injured (red), and Merged (combined clusters, mixed colours), along with the marker genes *Satb2*, *Lrp8*, *Etv1*, *Tnn1*, *Crym*, *Mrp11* marking the L5 ET clusters. (C) The bar graph (top) represents the number of chromatin accessibility peaks identified as significantly upregulated (green) and downregulated (red) post-injury in snATAC-seq analysis. Pie chart (bottom left) illustrates the genomic distribution of the upregulated peaks, with 74.4% located in potential enhancer regions and 25.6% in promoters. The histogram (bottom right) depicts the log2 fold-change distribution of upregulated peaks, with the majority exhibiting moderate fold changes. (D) Left panel bubble-plot shows clustered GO terms in two-dimensional semantic space, with circle size representing gene count and colour intensity indicating statistical significance (-log10 p-value). Right panel

displays the percentage of unique injured peaks associated with key biological processes. (E) Radar chart comparing the magnitude and distribution of chromatin accessibility changes in injured (red) neurons across six key biological pathways. The concentric circles represent Log2FC values ranging from 0.5 to 4.0. (F) Heatmap showing gene expression activity across key biological pathways as determined by GO term analysis. The vertical axis represents genes sorted by Log2FC values, while the horizontal axis displays the six major pathways. Colour intensity corresponds to Log2FC values according to the scale bar (right), with darker green indicating higher accessibility (p-value <0.05, Bonferroni correction). (G) Circular-bar plots showing the distribution of chromatin accessibility peaks based on their Log2 fold change (Log2FC) magnitudes across six key biological pathways. Each plot displays the angular position representing the magnitude of fold change (ranging from 0.5 to 5.5), which is also signified by the intensity of green shading. The radial bars indicate the number of differential accessibility peaks at each fold change value for the pathways.

**Lesion proximity amplifies chromatin reopening across all growth pathways**

Lesion distance from the soma may limit the strength of injury-evoked growth programmes, so we compared the thoracic crush with a 350 micrometre intracortical micro-stab injury (ICI) that transects corticospinal axons within the motor cortex (Supplementary Figure S6-A-C). Nuclei harvested seven days after ICI were processed side-by-side with the thoracic cohort for snATAC-seq, using the same L5 ET identification strategy described above (Figure 3A; Supplementary Table S4). Representative histology demonstrating the thoracic crush injury and extent is shown in Supplementary Figure S5-A-B.

ICI increased the number of accessibility gains from 5,482 to 13,084, while losses numbered 1,390 (Figure 3B; Supplementary Table S4). Fold-change values also shifted upward: gains after thoracic injury seldom exceeded a log2 change of 2.5, whereas ICI peaks were largely distributed between log2 3 and 4 (Figure 3C; Supplementary Table S4). Pathway tallies reflected this difference; injury-responsive axon-guidance elements rose from 36 to 411, chromatin-remodelling from 51 to 394, cytoskeleton organisation from 40 to 296, nervous-system development from 49 to 619, and regulation of cell growth from 103 to 1,669 (Figure 3D-E; Supplementary Table S4). Median log2 gains increased in parallel; for example, axon-guidance enhancers moved from roughly 1.2 after crush to about 3.3 after ICI. Genome-browser views at *Cntn2*, *Nrp1*, *Actb1*, *Stmn4*, and *Tubb2a* showed reopening of promoters together with multiple distal enhancers only in the cortical-injury condition (Figure 3F;

Supplementary Table S4). Footprint analysis was consistent with these patterns: PATZ1, SP1/2/3, and several KLF motifs were prominent after ICI but weak or undetectable after thoracic crush (Figure 3G; Supplementary Table S4). Collectively, these data indicate that bringing the lesion closer to the soma markedly increases both the number of accessible regions and their fold-change across all growth-related pathways.

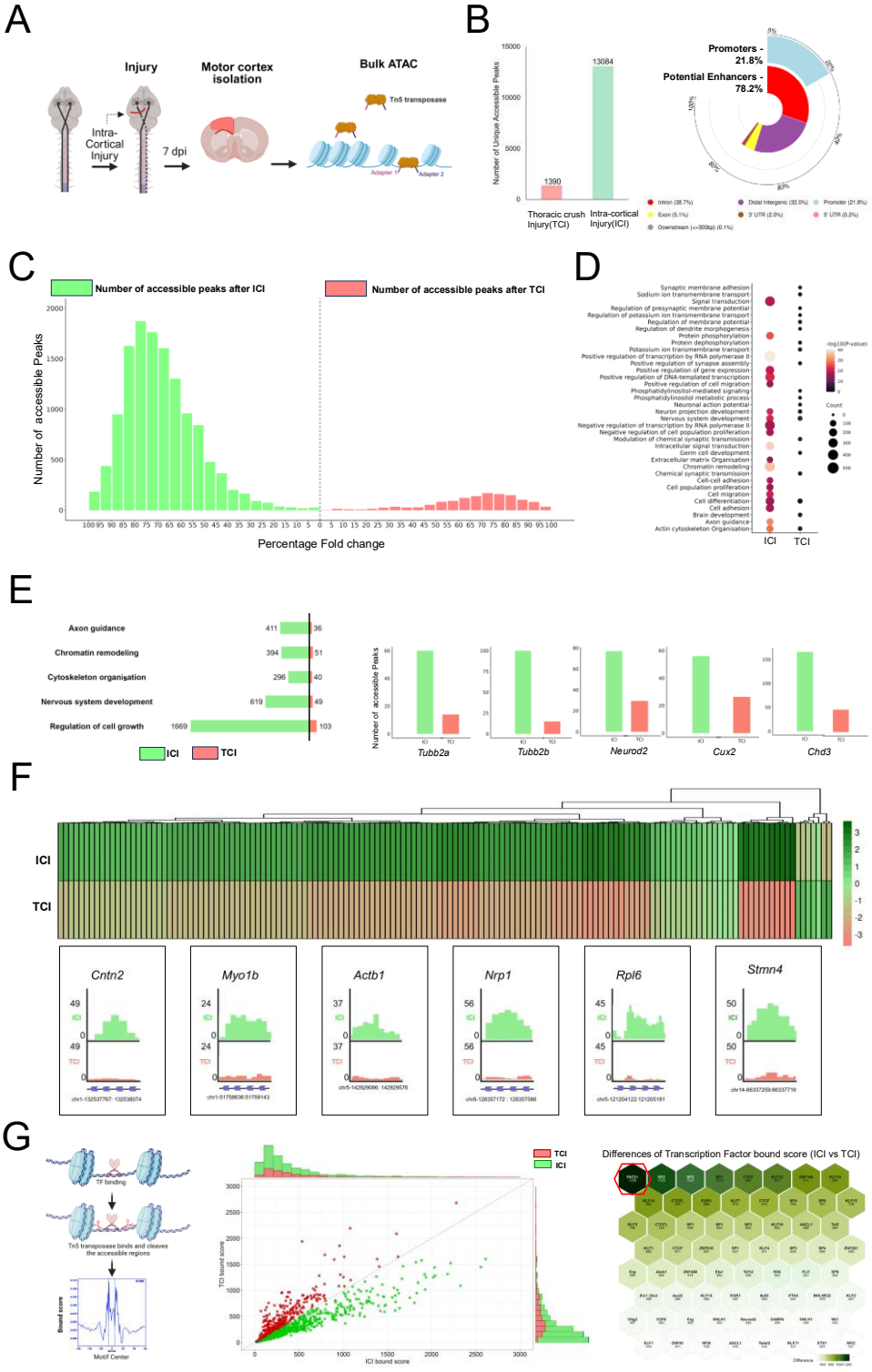

**Figure 3. ATAC-seq reveals injury site proximity affects the re-opening of key loci six-fold.** (A) Experimental workflow for ATAC-seq profiling after Intra-cortical Injury (ICI). (B) Quantification of accessible chromatin regions. Bar graph compares Thoracic crush injury (TCI) (1,390 peaks) versus ICI (13,084 peaks). Pie chart shows genomic distribution with enhancers (78.2%) and promoters (21.8%). (C) Distribution of accessible peaks by percentage fold change between injury models. ICI samples (green) show higher peak numbers with a maximum of 80-85% fold change compared to TCI samples (red). (D) Gene ontology (GO) analysis of differentially accessible regions. Dot plot shows enriched pathways with colour indicating significance (-log10(P-value)) and size showing gene count. ICI samples show greater enrichment in neuronal processes compared to TCI. (E) Pathway and gene-specific accessibility comparison. Left: Key neurobiological pathways show consistently higher accessibility in ICI versus TCI. Right: Neuronal genes (Tubb2a, Tubb2b, Neurod2, Cux2, Chd3) display greater accessibility in ICI than in TCI. (F) Pro-growth gene accessibility profiles. Top: Heatmap showing clustering of accessibility (green = increased). Bottom: UCSC browser tracks of six representative pro-growth genes showing higher accessibility peaks in ICI (green) versus TCI (red). (p-value <0.05). (G) Left: Schematic illustration of TF footprinting analysis showing TF binding to DNA and Tn5 transposase cleavage of accessible regions, resulting in characteristic footprint patterns. Center: Scatter plot comparing IC bound scores (x-axis) vs TC bound scores (y-axis) with marginal histograms, demonstrating differential TF binding between injury conditions. Right: Hexplot visualisation of the differences in transcription factor binding scores between ICI and TCI conditions. The colour intensity (light to dark green) represents the magnitude of difference, with the darkest hexagons (e.g., PATZ1, SP2) indicating transcription factors with the greatest differential binding between conditions.

## Developmental loss and injury-dependent resurgence nominate PATZ1 as a candidate chromatin regulator

Motivated by the observation that proximal injury restores extensive enhancer accessibility, we searched for transcription factors whose developmental decline and injury-dependent recovery might correlate with this difference. We analysed 616 vertebrate motifs with TOBIAS footprinting across the embryonic-to-adult ATAC-seq series and ranked them by footprint abundance, loss between P0 and adulthood, and gain after intracortical relative to thoracic injury (Supplementary Figure S7-A-B). Intersecting the highest-scoring motifs with the growth-gene enhancer set highlighted PATZ1. At E18 and P0, PATZ1 footprints numbered

826 and 801, respectively; counts fell to 462 at P4, 119 at P7, and 27 in the adult cortex, representing a 97% reduction. After intracortical injury, 644 PATZ1 footprints reappeared, whereas thoracic crush restored only 88. Co-occupancy analysis showed that 72% of PATZ1 sites lay within 25 bp of SP1 or SP2 motifs and 61% within 50 bp of KLF7 or KLF4 motifs, a configuration associated with GC-rich stripe elements (Supplementary Figure S7-C). Stripe factors are transcription factors that bind to GC-rich sequences and are thought to help define regulatory domains by clustering at active enhancers and promoters; they often co-occupy sites and may act cooperatively to maintain open chromatin. The PATZ1-bound enhancers mapped to genes involved in axon extension, cytoskeletal regulation, chromatin organisation, DNA repair, and growth signalling, the same pathways that reopen most strongly after proximal injury (Supplementary Figure S7-D). These converging patterns nominated PATZ1 as a candidate regulator whose presence correlates with, and may contribute to, the more extensive chromatin access achieved when the lesion is close to the soma.

Immunohistochemical analysis confirmed that PATZ1 protein is expressed in postnatal day 0 (P0) mouse brain but substantially reduced in adult brain (Supplementary Figure S8-A-B). Quantification of PATZ1 fluorescence intensity revealed significantly higher expression in P0 samples compared to adult brain (Supplementary Figure S8-D), consistent with the developmental decline observed in footprinting analysis.

**Exogenous PATZ1 expression elevates chromatin accessibility after distal injury**

Loss of PATZ1 footprints in the adult and their strong resurgence after intracortical injury suggested that reintroducing this factor might elevate the epigenetic response to a thoracic lesion toward the proximal-injury benchmark. To test this idea, we packaged full-length murine PATZ1 under a CAG promoter in AAV9 with a P2A-GFP reporter (AAV9-CAG-PATZ1-P2A-GFP), enabling identification of transduced cells by GFP fluorescence. We injected the vector bilaterally into layer V motor cortex and performed a complete T8 crush two weeks later. A separate cohort received AAV9-CAG-GFP (control vector lacking PATZ1) followed by the same injury. Motor cortices were collected seven days after injury, and GFP-positive nuclei were isolated by FANS before generating 3' snATAC-seq libraries (Figure 4A). We focused on the injured condition because our primary question was whether PATZ1 could enhance the injury response; comparison with the developmental data and with uninjured adult cortex (presented above) provides the relevant baselines.

Representative images confirming AAV transduction in layer V motor cortex are shown in Supplementary Figure S9-A. Colocalization of PATZ1 and GFP signals confirmed successful overexpression in transduced neurons (Supplementary Figure S8-C). Quantitative analysis by qPCR demonstrated robust PATZ1 overexpression compared to controls (Supplementary Figure S9-B-C).

snATAC-seq library quality for injured and PATZ1-injured samples was confirmed by TSS enrichment and fragment size distribution (Supplementary Figure S10-A-B). UMAP visualization revealed distinct chromatin accessibility profiles between conditions, with CST and non-CST populations identified (Supplementary Figure S10-C-D). Cell type-specific chromatin accessibility markers confirmed successful identification of neuronal populations (Supplementary Figure S10-E-F).

PATZ1 changed the distal-injury landscape both quantitatively and qualitatively. In PATZ1-positive nuclei, we detected 9,843 accessibility gains and 5,482 losses relative to GFP-control injured cortex (Figure 4B; Supplementary Table S6). The median log2 fold change for gained peaks doubled from 1.4 in GFP-control nuclei to 3.0 in PATZ1-expressing cells, and the high-amplitude tail expanded markedly: 7,022 peaks exceeded log2 4 after PATZ1, whereas only 71 did so in GFP controls. Consistent with PATZ1's stripe-factor profile, 78% of new gains resided within distal enhancer annotations.

All core growth pathways showed increased accessibility with PATZ1, although the magnitude varied across categories. Axon-guidance peaks that gained accessibility rose from about 128 to 287; chromatin-remodelling peaks from roughly 72 to 214; cytoskeleton-organisation peaks from around 63 to 153; nervous-system-development peaks from about 59 to 266; and regulation-of-cell-growth peaks from approximately 112 to 524 (Figure 4C-D; Supplementary Table S6). Circular ridge-line plots showed a parallel shift toward higher fold-change values in every pathway, with the majority of peaks now falling between log2 2 and log2 4 (Figure 4E; Supplementary Table S6). Hierarchical clustering further divided the differential peaks into two principal branches: a large group of 6,814 loci that opened only when PATZ1 was present and was enriched for PATZ1, SP, and KLF motifs, and a smaller group that responded to injury irrespective of PATZ1 expression (Figure 4F-G; Supplementary Table S6).

In summary, forced expression of PATZ1 converts the muted chromatin response to a distal spinal lesion into a profile that approaches the magnitude and breadth achieved by a proximal cortical injury, markedly increasing both the number of accessible regions and their fold change across all growth-related pathways.

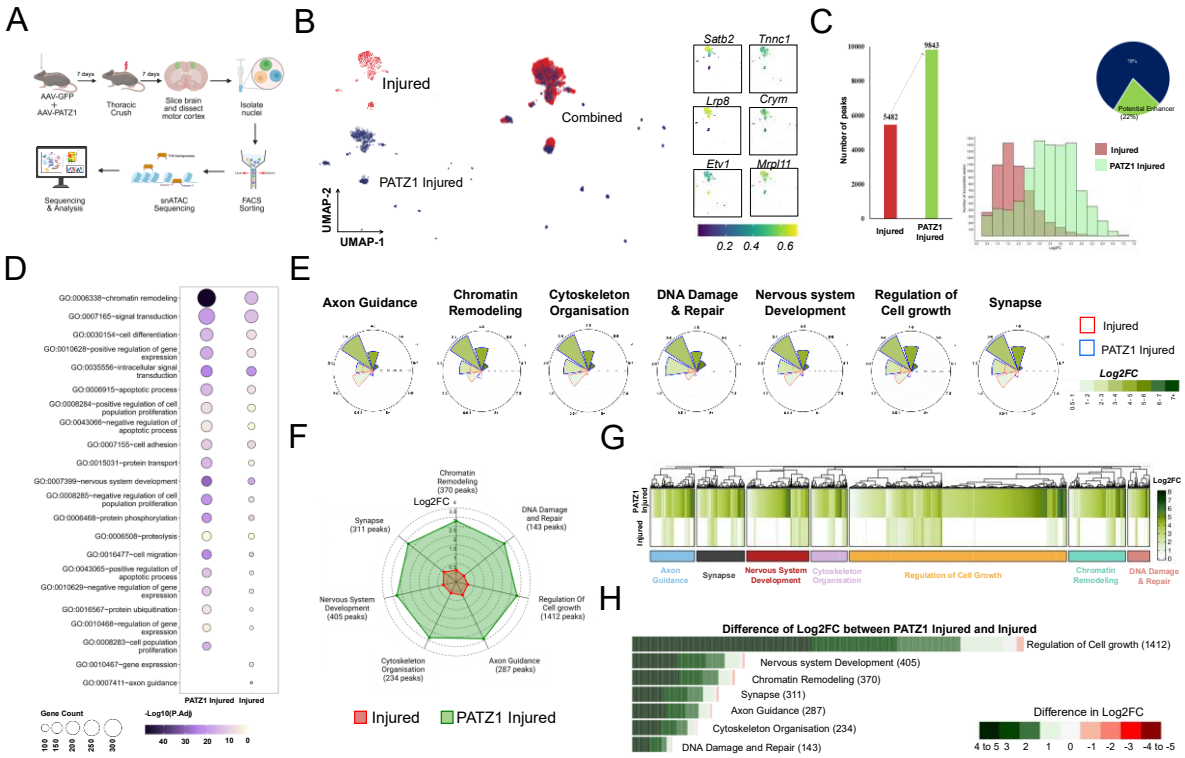


**Figure 4. Single-nuclear (sn)ATAC-seq reveals that chromatin around pro-growth genes becomes more accessible upon PATZ1 over-expression.** (A) Schematic representation of single-nucleus ATAC-seq (snATAC) experimental workflow with AAV-PATZ1. (B) UMAP representation showing distinct clustering patterns between Injured control and PATZ1_Injured conditions. (C) Quantitative analysis demonstrating increased accessible chromatin regions in PATZ1 overexpression (9843) versus Injured control (5482). Pie charts displaying the genomic distribution of the PATZ1 over-expressed peaks. Histogram showing the number of accessible peaks in injured control (red) and upon PATZ1 over-expression (green). (D) Dot plot showing Top 20 Gene Ontology (GO) terms in PATZ1-overexpression versus injured control conditions. The size of dots represents the number of genes associated with each GO term, while colour intensity indicates statistical significance (-log10 p-value). (E) Circular plots comparing chromatin accessibility patterns between PATZ1-overexpressing (Blue bar) and control injured (orange bar) neurons across seven key biological pathways. Each plot displays the distribution of differential accessibility based on Log2 fold change (radial axis

from 0 to 8), magnitude signified by the intensity of green shading. (F) Radar chart comparing the magnitude and distribution of chromatin accessibility changes between PATZ1-overexpressing (green) and control injured (red) neurons across seven key biological pathways. Each axis represents a distinct pathway, with the total number of associated accessible peaks indicated in parentheses. The concentric circles represent Log2FC values ranging from 0.5 to 4.0. (G) Heatmap of differential accessibility across neuronal pathways, with colour intensity representing fold change. Colour intensity (green) represents fold change in accessibility, with annotated functional pathways (p-value <0.05, Bonferroni correction, FDR <0.05). (H) Horizontal bar graph displaying the difference in Log2FC values of chromatin accessibility between PATZ1-overexpressing and injured control neurons across seven key biological pathways. The colour scale ranges from dark green (strong positive difference, indicating greater accessibility in PATZ1-overexpressing neurons) to red (negative difference, indicating reduced accessibility).

**PATZ1 couples enhancer reopening to transcriptional changes after distal injury**

Because chromatin accessibility does not invariably translate into transcription, we next asked whether the expanded enhancer landscape produced by PATZ1 alters gene expression. Using matched samples from the same cohort analysed for snATAC-seq, we generated 3' single-nucleus RNA-seq (snRNA-seq) libraries and retained 9,871 L5 ET nuclei after quality control (Figure 5A). UMAP visualization of snRNA-seq data showed cell clusters in injured and PATZ1-injured conditions (Supplementary Figure S11-A-B). L5 ET neurons were identified by expression of marker genes including *Satb2*, *Crym*, and *Etv1* (Figure 5B; Supplementary Figure S11-C-D). Differential expression analysis relative to GFP-injured controls (FDR < 0.05; |log2FC| at least 0.5) identified 1,825 upregulated and 4,369 downregulated genes (Figure 5C).

To characterise the relationship between PATZ1-induced chromatin accessibility and transcriptional activation, we performed integrative analysis of snATAC-seq and snRNA-seq data (Figure 5D-E; Supplementary Table S7). For upregulated genes, we identified 4,483 accessible regions not associated with differential gene expression, 523 regions both accessible and transcriptionally active, and 1,131 differentially expressed genes without detectable chromatin accessibility changes. For downregulated genes, we identified 4,199 accessible peaks without transcriptional changes, 807 accessible regions with decreased expression, and 2,504 genes with decreased expression but no accessibility changes.

Plotting fold changes for the 523 upregulated and 807 downregulated genes by accessibility (snATAC) versus transcription level (snRNA) revealed that most upregulated genes fell within the low transcription bin (0.5 to 1 log2FC) and downregulated genes within the very low bin (-2 to -4 log2FC) (Supplementary Figure S12-A; Supplementary Table S7). This modest transcriptional output despite robust chromatin opening suggests that while PATZ1 may establish a permissive chromatin state, maximal transcriptional activation likely requires additional pro-growth transcription factors acting in combination.

Gene Ontology analysis of accessible and differentially expressed genes revealed distinct functional signatures (Figure 5F; Supplementary Table S7). Among upregulated genes, PATZ1 expression was associated with activation of neuronal differentiation programmes and translational control machinery, including ribosome biogenesis, regulation of translation, and RNA processing. Broadly, activated pathways converged on nervous system development, transcriptional regulation, signal transduction, synaptic function, growth regulation, chromatin remodelling, axon guidance, cytoskeleton organisation, and calcium ion signalling. This pattern suggests that PATZ1 primes neurons toward a growth-competent state by simultaneously opening developmental gene programmes and enhancing the translational capacity needed to support axon extension.

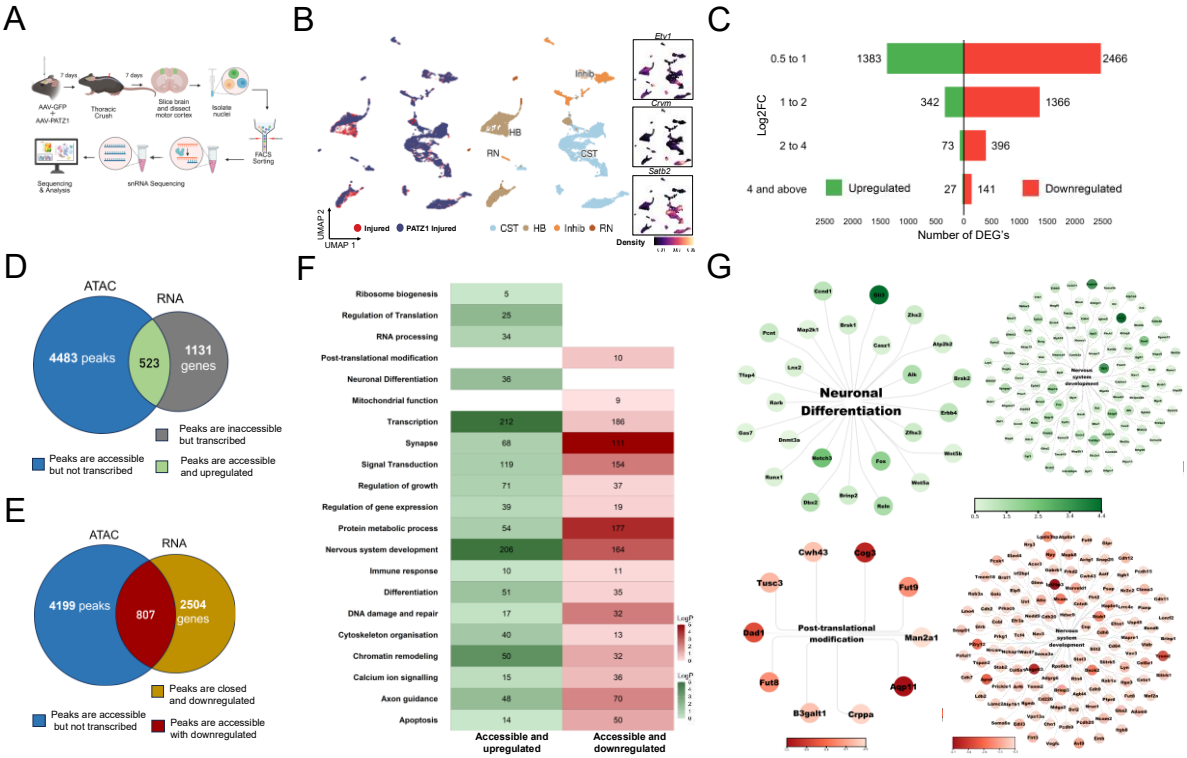

**Figure 5. Integrative analysis of single-nucleus RNA sequencing and ATAC sequencing reveals transcriptional and chromatin accessibility profiles in PATZ1 tissue sample.** (A) Schematic illustration of the experimental workflow. (B) UMAP visualisation of single-nucleus RNA-seq (snRNA-seq) data from the PATZ1 sample. (C) Distribution of differentially expressed genes (DEGs) by fold change categories. The horizontal bar plot displays the number of upregulated (green) and downregulated (red) genes across four log2 fold-change ranges (0.5 to 1, 1 to 2, 2 to 4, and 4 and above), indicating the exact count of DEGs within each category. (D)Left: Venn diagram showing the overlap between accessible chromatin peaks identified by ATAC-seq (4483 peaks) and transcribed genes identified by RNA-seq (1131 genes), with 523 features showing both accessibility and transcription. (E) Left: Venn diagram identifying peaks accessible but not transcribed (blue), accessible with increased expression (red, 807 peaks), and closed with decreased expression (yellow, 2504 genes). (F) Heatmap showing Gene Ontology (GO) enrichment analysis of Accessible and differentially expressed genes. The left panel displays accessible and upregulated pathways (green bars), while the right panel shows accessible and downregulated pathways (red bars). Numbers within each bar indicate the count of genes associated with each biological process, and the gradient colour represents logP value from 0(light green) to 5(dark green). (G) Network visualization of gene interactions within selected biological processes. The upper panel illustrates the neuronal differentiation and nervous system development network with genes shown as nodes connected by edges representing functional interactions. The lower panel depicts the post-translational modification and nervous system development network. The gradient color scale represents the log2 fold change (logFC) values from snRNA-seq data, with green indicating upregulated genes and red indicating downregulated genes, where color intensity reflects the magnitude of differential expression.

Conversely, PATZ1 was associated with repression of protein metabolic processes and post-translational modification pathways, alongside mild suppression of mitochondrial function. Repressed pathways also included subsets of synaptic, axon guidance, and signal transduction genes, as well as transcriptional programmes, nervous system development genes, and cell survival and stress pathways including apoptosis and DNA damage repair. This bidirectional pattern, with activation of some developmental and guidance genes alongside repression of others, suggests that PATZ1 does not uniformly upregulate growth programmes

but rather reshapes the transcriptional landscape, potentially suppressing mature neuronal identity genes while reactivating earlier developmental programmes.

Consistent with this interpretation, developmental expression profiling of neuronal differentiation genes upregulated by PATZ1 showed that these genes, including *Brinp2*, *Casz1*, *Notch3*, *Runx1*, *Wnt5a*, and *Zfhx2*, are highly expressed during embryonic and early postnatal stages but decline toward adulthood (Supplementary Figure S12-B). Genome browser tracks at representative loci further illustrated the selective nature of PATZ1 action: upregulated nervous system genes such as *Sema3f* and *Cux2* showed concordant PATZ1 binding, increased accessibility, and elevated expression, whereas downregulated genes such as *Pcdh9* and *Col8a1* showed reduced accessibility and expression upon PATZ1 binding, demonstrating selective regulation of distinct nervous system gene subsets (Supplementary Figure S12-C).

Consistent with the observation that transcriptional responses to PATZ1 alone are modest, we tested whether PATZ1 overexpression by itself, without additional pro-growth factors, could promote axonal sprouting in a pyramidotomy model. AAV-PATZ1 or AAV-GFP was injected into motor cortex, followed by unilateral pyramidotomy 60 days later, and corticospinal axon sprouting was quantified in coronal spinal cord sections at increasing distances from the lesion border (Supplementary Figure S15-A). CST labelling was confirmed with medullary pyramids, and pyramidotomy was verified by PKCγ immunohistochemistry (Supplementary Figure S15-B). Qualitative examination of GFP-labelled corticospinal axons suggested a trend toward increased sprouting in AAV-PATZ1-treated animals compared to AAV-GFP controls (Supplementary Figure S15-C). Quantification of fibre index at increasing distances from the pyramidotomy lesion (0-200 μm, 200-400 μm, 400-600 μm, and greater than 600 μm) revealed a trend toward increased sprouting at larger distances from the midline in PATZ1-treated animals, but this difference was not statistically significant (Supplementary Figure S15-D-E). Two-way ANOVA revealed a significant main effect of distance ($F(3,9) = 9.689$, $P = 0.0035$), indicating progressive decrease in fibre density with increasing distance from the lesion, but no significant main effect of PATZ1 ($P = 0.4497$) or interaction between PATZ1 and distance ($P = 0.8538$). These findings suggest that while PATZ1 establishes a permissive chromatin landscape, additional pro-growth transcription factors may be required in combination to achieve robust axonal regeneration.

**PATZ1 enhances enhancer acetylation and alters CTCF distribution after distal injury**

To mechanistically dissect PATZ1-mediated epigenetic priming, we sought to determine whether the chromatin accessibility changes observed upon PATZ1 overexpression are accompanied by deposition of active enhancer marks and reorganisation of architectural boundaries. We performed CUT&RUN profiling for H3K27ac (a marker of active enhancers) and CTCF (an insulator protein that demarcates topological domains) in motor cortex tissue following thoracic crush injury (Supplementary Figure S13-A).

We first established a baseline by examining how injury alone affects these chromatin marks in the absence of PATZ1 overexpression. Comparing thoracic-injured cortex with uninjured controls, H3K27ac profiling revealed 483 regions unique to uninjured tissue, 690 overlapping regions, and 444 regions unique to injured tissue (Supplementary Figure S13-B). Representative genome browser tracks at loci such as *Fosb* promoter and *Cdh11* intron illustrate these dynamics (Supplementary Figure S13-B). Gene Ontology analysis showed that H3K27ac-lost regions were enriched for regulation of transcription by RNA polymerase II, nervous system development, and chromatin remodelling, while H3K27ac-gained regions were enriched for cell adhesion, intracellular signal transduction, extracellular matrix organisation, and neurogenesis (Supplementary Figure S13-C-D). The genomic distribution of differentially marked H3K27ac sites showed that most changes occurred at distal regions, with both gained and lost peaks distributed across distances from transcription start sites (Supplementary Figure S13-E).

CTCF profiling revealed a similarly balanced redistribution upon injury: 725 regions were unique to uninjured tissue, 1,008 were shared, and 1,421 were unique to injured tissue (Supplementary Figure S13-F). Representative tracks at *Rara* promoter and *Cdk20* intergenic regions demonstrate these boundary shifts (Supplementary Figure S13-F). Lost CTCF sites were enriched for negative regulation of DNA-templated transcription, regulation of DNA-templated transcription, and intracellular signal transduction, whereas gained CTCF sites were associated with negative regulation of apoptotic process, cell migration, and positive regulation of gene expression (Supplementary Figure S13-G). Analysis of GO pathways enriched in both lost and gained CTCF binding sites revealed that signal transduction, regulation of transcription, chromatin remodelling, and cell differentiation pathways showed bidirectional CTCF reorganisation upon injury (Supplementary Figure S13-H). Together, these data confirm that distal injury triggers a balanced yet modest reshaping of enhancer marks and insulator boundaries, providing a baseline against which PATZ1-driven remodelling can be assessed.

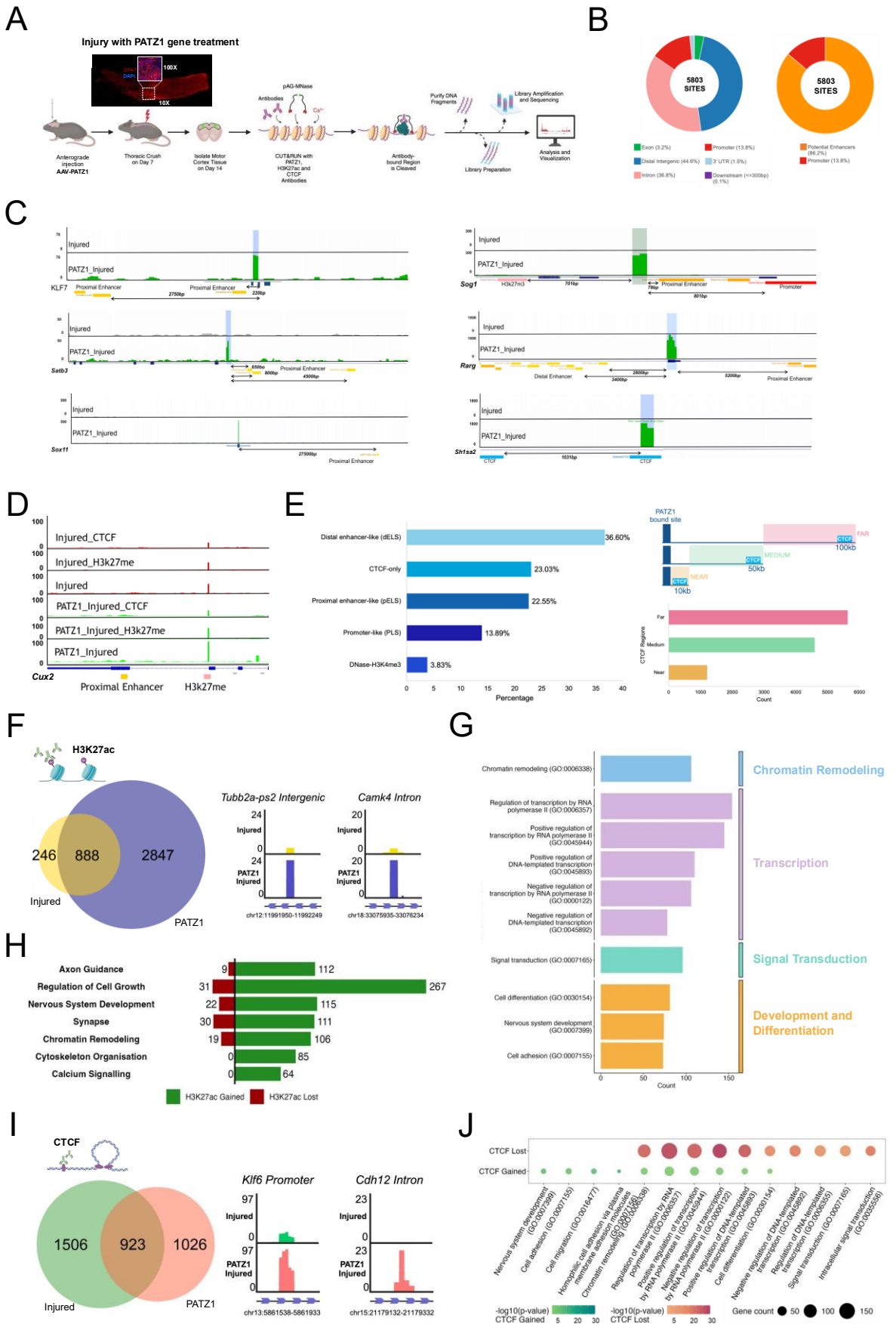


**Figure 6. Genome-wide profiling of PATZ1 binding sites using CUT&RUN.** (A)

Schematic of the CUT&RUN workflow for mapping PATZ1 binding sites, CTCF and H3k27ac marks. (B) Genomic distribution of 5803 PATZ1-bound sites. Left: Distribution across genomic features showing Exon (3.2%), Distal Intergenic (44.6%), 5' UTR (1.8%), Intron (36.8%), and Downstream (<300bp) (9.1%). Right: Regulatory element classification showing Potential Enhancers (86.2%), Promoters (13.8%), and TTS (0.1%).(C) Genome browser tracks showing PATZ1-induced chromatin accessibility at pro-growth genes. Left panel: Representative loci (*Klf7*, *Satb3*, *Sox11*) showing increased chromatin accessibility in PATZ1-injured (green) compared to injured control (blue). Right panel: Additional loci (*Sgo1*, *Rarg*, *Sh1sa2*) with enhanced accessibility. Yellow bars indicate proximal or distal enhancers; blue boxes mark CTCF binding sites. Black arrows indicate genomic distances and enhancer locations relative to gene bodies.(D) Detailed view of PATZ1 binding, CTCF occupancy, and H3K27ac marks at the *Cux2* locus. Tracks show Injured_CTCF (red), Injured_H3K27me (red), Injured control (red), PATZ1_Injured_CTCF (green), PATZ1_Injured_H3K27me (green), and PATZ1_Injured (green). Yellow bars indicate proximal enhancer and H3K27me regions. (E) Distribution and characterization of PATZ1 binding at cis-regulatory elements. Left: Percentage distribution showing distal enhancer-like (dELS, 36.60%), CTCF-only (23.03%), proximal enhancer-like (pELS, 22.55%), promoter-like (PLS, 13.89%), and DNase-H3K4me3 (3.83%). Right: CTCF motif enrichment relative to PATZ1 binding sites categorized by binding strength (Far: pink, >100kb; Medium: green, 50kb; Near: orange, <10kb), with count distribution shown on x-axis.(F) Overlap of H3K27ac-enriched regions between injured (246 unique) and PATZ1-treated injured samples (2847 unique), with 888 shared regions. Right: Browser views showing PATZ1-dependent H3K27ac enrichment (blue) compared to injured-only samples (yellow). (G) GO analysis of H3K27ac regions unique to PATZ1-treated injured samples. (H) Regeneration-associated pathways enriched in H3K27ac-marked regions: gained (green) and lost (red) in PATZ1-treated injured samples. (I) Overlap of CTCF binding sites between injured (1506 unique) and PATZ1-treated injured (1026 unique) samples, with 923 shared sites. Right: Browser tracks showing condition-specific CTCF peaks. (J) GO analysis showing pathways with CTCF lost (pink) and gained (green) between conditions. Dot size: gene count; colour intensity: significance (-log10(p-value).

Given this modest baseline response to injury, we next asked whether PATZ1 overexpression could drive more extensive chromatin remodelling. A widened ATAC footprint can reflect

either direct binding by the introduced factor or secondary recruitment of chromatin modifiers, so we examined whether PATZ1 occupies the newly opened regions and whether its presence is accompanied by enhanced H3K27ac deposition or alterations in CTCF distribution. We generated CUT&RUN libraries from a separate cohort of animals that received either AAV-PATZ1 or AAV-GFP, followed by thoracic crush, and harvested on post-injury day 7.

We first validated CUT&RUN antibody performance. AAV-PATZ1-GFP injection targeting and transduction in layer 5 motor cortex neurons was confirmed by immunofluorescence (Supplementary Figure S14-A). For CTCF, we confirmed appropriate nuclear localisation in both control and PATZ1 overexpression conditions at 40x and 100x magnification (Supplementary Figure S14-B). For H3K27ac, we verified nuclear localisation consistent with active chromatin marks in both conditions (Supplementary Figure S14-C). These quality control analyses support the reliability of our CUT&RUN data.

CUT&RUN with a PATZ1 antibody identified 5,803 binding sites in PATZ1-overexpressing injured cortex (Figure 6A-B; Supplementary Table S9). Genomic distribution analysis revealed that 86.2% of these sites lay within regulatory regions classified as potential enhancers, with the remaining 13.8% at promoters (Figure 6B). Genome browser tracks at pro-growth genes including *Klf7*, *Satb3*, *Sog1*, *Rarg*, *Sh1sa2* and *Sox11* illustrated PATZ1 binding at intergenic regions overlapping ENCODE-annotated regulatory elements and distal enhancers (Figure 6C). Additional examples at *Cux2* promoter regions demonstrated PATZ1 binding patterns, CTCF occupancy and H3k27ac marks in PATZ1 treated samples (Figure 6D). Classification of PATZ1-bound cis-regulatory elements showed that distal enhancer-like regions comprised the largest fraction (36.60%), followed by CTCF-only sites (23.03%), proximal enhancer-like regions (22.55%), promoter-like regions (13.89%), and DNase-H3K4me3 sites (3.83%). Motif analysis revealed enrichment of CTCF motifs at specific distances from PATZ1 binding sites (Figure 6E).

H3K27ac profiling in the same samples revealed that PATZ1 expression was associated with 2,847 new acetylation peaks compared to GFP-control injured cortex, while only 246 were lost (Figure 6F; Supplementary Table S9). Notably, 94% of these de novo H3K27ac sites centred within plus or minus 250 bp of a PATZ1 summit, and 81% overlapped enhancers linked to genes upregulated in the snRNA-seq dataset. Browser tracks at *Tubb2a-ps2* and *Camk4*, illustrate the tight spatial coupling between PATZ1 occupancy and de novo H3K27ac signal (Figure 6F-G). Functional grouping of the acetylation gains highlighted transcriptional

regulation, chromatin organisation, nervous-system development, and axon guidance, mirroring the categories that gained accessibility in the snATAC-seq dataset (Figure 6H; Supplementary Table S9).

We then profiled CTCF to assess whether PATZ1 influences domain boundaries. Relative to GFP-control injured cortex, PATZ1-expressing tissue gained 1,026 new CTCF peaks and lost 1,506, leaving 923 shared sites (Figure 6I-J; Supplementary Table S9). Newly acquired CTCF binding occurred preferentially within 50 kb of genes involved in cell adhesion, axon guidance, whereas lost sites clustered near transcriptional repressors and differentiation inhibitors. Motif-distance analysis revealed an over-representation of CTCF motifs 120 to 180 kb away from PATZ1 summits, suggesting that enhancer activation by PATZ1 is accompanied by repositioning of distal insulator boundaries rather than wholesale redistribution across the genome.

In summary, PATZ1 binds directly to thousands of distal enhancers opened after injury, and this binding is associated with H3K27ac deposition at those sites and selective reorganisation of CTCF boundaries around growth-related loci. These data provide biochemical evidence that PATZ1 converts accessible chromatin into functionally marked enhancer domains while modifying higher-order insulation to potentially facilitate long-range regulatory contacts.

**PATZ1 is associated with three-dimensional genome reorganisation at growth loci**

Our CUT&RUN data indicated that PATZ1 alters local enhancer marks and CTCF positioning, but whether these changes propagate into higher-order chromatin topology remained unknown. To address this question, we prepared Hi-C libraries from a matched cohort of AAV-PATZ1 and AAV-GFP mice that had undergone thoracic crush and were harvested on day 7 (Figure 7A). Each sample yielded approximately 800 million valid contacts, which were ICE-balanced at 10 kb resolution before downstream analysis.

Genome browser tracks at axon growth genes including *Tubb2a*, *Sgo1*, and *Icam1* revealed differences in three-dimensional chromatin organisation between PATZ1-injured and injured control samples (Figure 7B). These tracks integrate TAD boundaries, CTCF binding, active enhancer and promoter marks (H3K27ac), regulatory factor binding, chromatin accessibility (ATAC-seq), and transcriptional activity, with loops indicating chromatin interactions between regulatory elements.

Eigenvector decomposition revealed selective compartment switching in PATZ1-expressing cortices: 3,557 regions (3.5% of total) moved from inactive B to active A compartment, whereas 2,949 regions (2.9%) shifted from A to B (Figure 7C). Although numerically modest, these transitions were functionally skewed. Gene Ontology analysis of the top 10 enriched terms showed that B-to-A compartment switches were associated with energy homeostasis, cell adhesion, apoptotic process, inflammatory response, signal transduction, chromatin remodelling, nervous system development, regulation of transcription, metabolic process, and proteolysis (Figure 7D, left). Conversely, A-to-B compartment switches were enriched for negative and positive regulation of transcription by RNA polymerase II, regulation of cell population proliferation, negative regulation of DNA-templated transcription, negative regulation of apoptotic process, chromatin remodelling, and cell differentiation (Figure 7D, right). Thus, PATZ1 is associated with selective movement of growth-supportive loci into an active A-compartment environment while relegating certain regulatory genes to the inactive B compartment.

To examine the functional consequences of compartment switching, we assessed how many genes within B-to-A shifted regions showed corresponding changes in chromatin accessibility and transcription (Figure 7E). Of the 790 genes in shifted A compartment regions, 294 (38.0%) showed differential accessibility, and 9 (3.1%) were differentially transcribed. Gene Ontology analysis of these differentially accessible genes within shifted compartments revealed enrichment for chromatin remodelling, nervous system development, signal transduction, and regulation of transcription (Figure 7F, Supplementary Table S10).

Boundary mapping using insulation-score minima identified distinct TAD categories: 1,319 conserved TADs, 1,052 injured-unique TADs, 2,500 PATZ1-unique TADs, and 2,602 shifted TADs (Figure 7G). Comparison of TAD properties between injured and PATZ1 conditions revealed differences in insulation ratio (IR) distribution, TAD length distribution, and log2 fold change in read counts (Figure 7H, Supplementary Table S10). Newly created TADs in PATZ1 samples were significantly smaller, with the TAD length distribution shifted toward shorter domains compared to injured controls, indicating a compaction of loop architecture that concentrates regulatory communication around growth genes.

Together, these Hi-C data show that PATZ1 action extends beyond local chromatin: it is associated with targeted compartment flips, redrawn TAD borders, and compacted

interaction ranges, thereby embedding growth-associated loci within a three-dimensional framework that may favour enhancer-promoter communication.

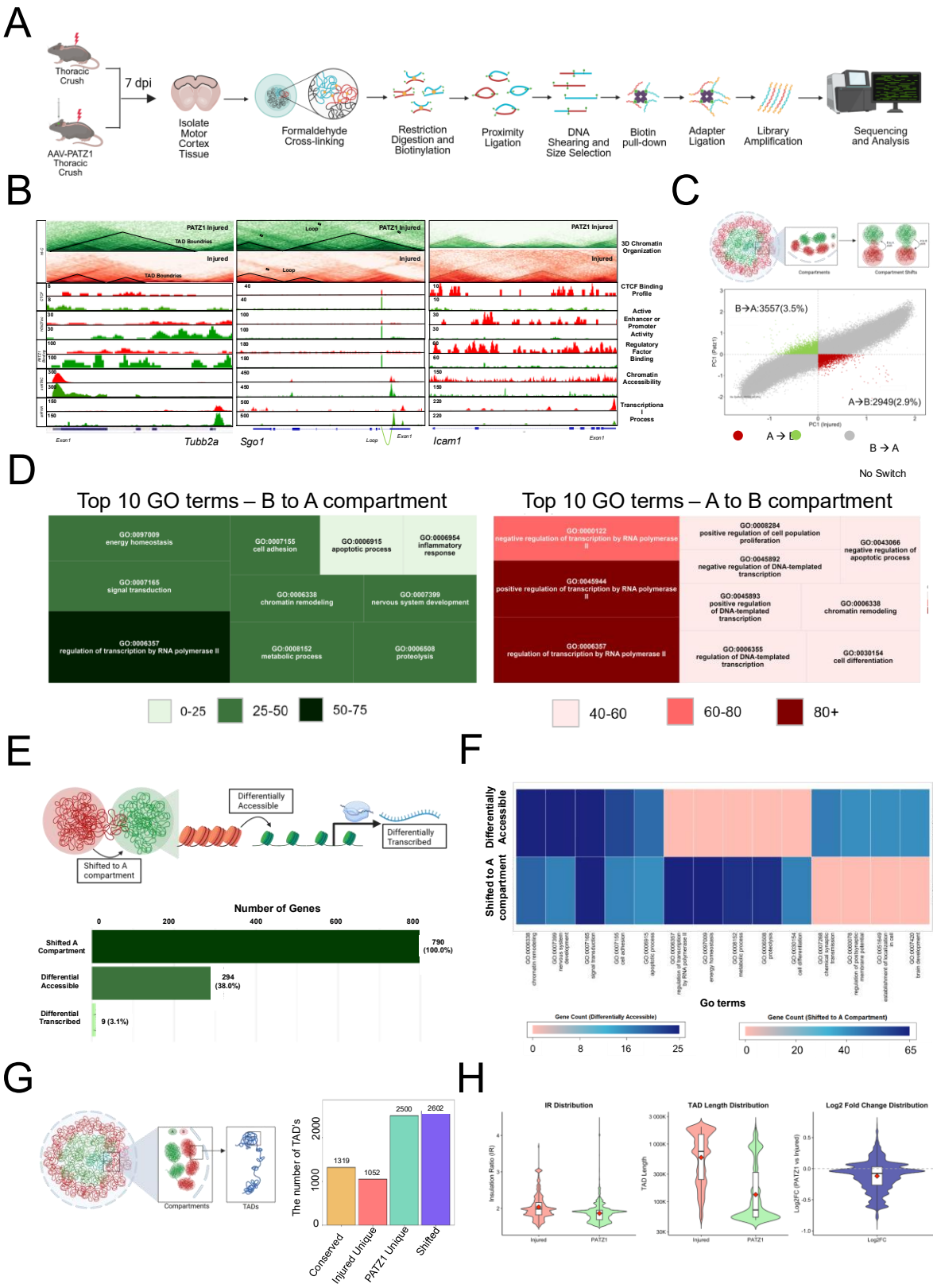

**Figure 7. Functional analysis of compartment switching by PATZ1.** (A) Experimental workflow for Hi-C analysis. (B) Genome browser tracks at axon growth genes (*Tubb2a, Sgo1, Icam1*) comparing PATZ1-injured (green) versus injured control (red) samples. Tracks show 3D chromatin organization with TAD boundaries (top), CTCF binding, active enhancer/promoter marks (H3K27ac), regulatory factor binding, chromatin accessibility (ATAC-seq), and transcriptional activity. Loops indicate chromatin interactions between regulatory elements. Gene structures shown below with exons as blue boxes.(C) Top: Depicts a model of nuclear organisation showing A/B compartmentalisation (green/red) and compartment shifts between conditions. Bottom: The bottom scatterplot shows principal component analysis of genomic regions, with points coloured by compartment switching status: B→A regions (3557 regions, 3.5% of total) in green, A→B regions (2949 regions, 2.9%) in red, and non-switching regions in gray. The x-axis shows principal component (PC) values of the injured condition, while the y-axis shows principal component (PC) values of the PATZ1 condition. (D) Hierarchical representation of the top 10 Gene Ontology (GO) terms enriched in B→A compartment switches (left, green) and A→B compartment switches (right, red). Colour intensity indicates gene count ($p<0.05$). (G) Quantification of Topologically Associating Domains (TADs) across categories showing conserved (1319), Injured-unique (1052), PATZ1-unique (2500) and shifted (2602). (H) Distribution comparisons between Injured (red) and PATZ1 (green) conditions: IR values(left), TAD lengths (middle), and Log2FC read counts (right).

## Discussion

During maturation, forebrain neurons pass through two abrupt "lock-down" waves that progressively seal the promoters and enhancers required for axon extension. Our multi-omic time-course shows that this loss of accessibility is mirrored by a staged withdrawal of GC-stripe factors, culminating in the near-complete disappearance of PATZ1 by adulthood. We note that our developmental bulk ATAC-seq data were generated from heterogeneous forebrain tissue, which captures accessibility across multiple cell types; cell-type-specific dynamics in corticospinal neurons specifically may differ from these population-level trends. Nevertheless, these data provide a framework for understanding broad chromatin restriction during CNS maturation.

When a complete thoracic lesion is placed far from the soma, only a modest fraction of growth-associated elements re-opens in layer 5 extratelencephalic (L5 ET) neurons; by contrast, an intracortical lesion delivered a few hundred micrometres from the cell bodies reactivates roughly an order of magnitude more sites, reinstating PATZ1 footprints and extensive enhancer activity. We acknowledge that L5 ET neurons, while enriched for corticospinal projection neurons, also include other subcortical projection populations, and our findings should be interpreted with this limitation in mind. These observations link chromatin plasticity to lesion proximity and nominate PATZ1 as a molecular correlate of that distance effect, consistent with earlier work in sensory and retinal systems where local injury elicits substantial enhancer priming, whereas distal damage does not[19,22,31,36].

Re-introducing PATZ1 after thoracic injury demonstrates that a single transcription factor can convert the muted distal response into a chromatin landscape approaching that seen after proximal injury. PATZ1 binds thousands of GC-rich enhancers, is associated with H3K27ac deposition, and correlates with altered CTCF distribution and inter-TAD architecture, producing selective B-to-A compartment shifts and smaller, growth-centred domains. The same genomic regions gain accessibility, acquire active histone marks, and exhibit elevated transcription, while immune and metabolic programmes are curtailed, echoing enhancer-focused effects reported for NR5A2/KLF6 combinations[20] and for cohesin-driven looping in peripheral regeneration[36]. These data extend the stripe-factor paradigm from in-vitro chromatin maintenance[39] to in-vivo epigenetic changes in mature CNS neurons, though the causal relationships between PATZ1 binding and downstream chromatin reorganisation remain to be fully elucidated.

Notably, despite this substantial chromatin remodelling, PATZ1 overexpression alone did not produce statistically significant axonal sprouting in our pyramidotomy model. This outcome is mechanistically consistent with our integrated transcriptomic analysis showing that chromatin opening is necessary but not sufficient for robust transcriptional activation. PATZ1 establishes a permissive epigenetic landscape by opening enhancers and reorganising chromatin architecture, but the appropriate pro-growth transcription factors are required to occupy these newly accessible sites and translate chromatin availability into meaningful transcription and axon growth. In this view, PATZ1 functions as an "epigenetic enabler" that lowers the barrier to gene activation without directly driving the growth programme itself. This distinction may help explain why previous efforts targeting individual pro-growth transcription

factors have yielded variable results: without prior chromatin priming, these factors may encounter closed regulatory elements that limit their efficacy. Loss-of-function studies with PATZ1 in the context of proximal injury would further strengthen this model and represent an important direction for future investigation.

The findings refine current regeneration models in three ways. First, they separate the breadth of the injury response from its depth: distal axotomy engages every growth pathway but with insufficient amplitude, implying that clinical gain may come from boosting cues that already exist rather than inventing new ones. Second, they place enhancer activation at the centre of that amplification. PATZ1's influence is overwhelmingly enhancer-biased and mirrors the enhancer-rich opening characteristic of regeneration-competent peripheral neurons[35]; enhancer priming therefore emerges as a quantitative hallmark of successful regrowth. Third, they couple local enhancer priming to large-scale topology: PATZ1-associated TAD compaction and compartment switching focus regulatory interactions on growth genes while insulating apoptotic regulators, paralleling observations that CTCF-YY1 complexes and cohesin loops guide long-range control of repair genes[22,36].

PATZ1 is a POZ/BTB and AT-hook domain-containing zinc finger protein with well-established roles in development, stem cell maintenance, and gene regulation[40–43]. Its expression is high during early neurogenesis, concentrated in proliferating neural progenitors of the neocortical neuroepithelium, and tapers off toward adulthood, though it remains detectable in neurogenic niches[41]. Genetic studies show that PATZ1 is essential for neural stem cell proliferation, with its loss leading to hypoplasia of periventricular region[43]. It also interacts with core pluripotency factors like Nanog and Pou5f1 to sustain embryonic stemness[40,42]. More recently, PATZ1 was identified as a member of the "stripe" transcription factor family, which binds GC-rich DNA to help maintain open chromatin, recruit additional transcription factors, and stabilise their binding at regulatory elements[39]. This chromatin-opening role aligns with our findings of PATZ1 binding at growth-associated loci and its association with chromatin reorganisation in injured CNS neurons.

Our data also connect PATZ1's function to a broader biological theme observed in regeneration-competent peripheral neurons, which transiently downregulate their subtype identity and activate a shared injury-response programme, a shift thought to reflect temporary cellular plasticity. PATZ1's dual roles in maintaining developmental plasticity and associating

with chromatin remodelling suggest it may be a key enabler of this regenerative switch, though direct functional evidence for this hypothesis awaits further testing.

Mechanistically, PATZ1 likely uses several cooperative layers: direct DNA binding at GC motifs, recruitment of p300/CBP to lay down H3K27ac, and interaction with CTCF or cohesin to influence chromatin boundaries. Its documented partnerships with *Nanog* and *Pou5f1* in stem cells[40–42] and its requirement for neonatal progenitor proliferation[43] align with a potential ability to re-establish juvenile-like chromatin states in differentiated neurons. The precise mechanism by which PATZ1 selectively targets growth-associated loci, rather than acting genome-wide, remains an open question; one possibility is that PATZ1 preferentially binds GC-rich sequences already marked by residual accessibility or specific histone modifications in adult neurons.

Perhaps the most significant contribution of this work is the identification of a targeted strategy to prime the epigenome for growth, an approach that has remained elusive in the CNS regeneration field. While considerable effort has been devoted to identifying and delivering pro-growth transcription factors, the chromatin landscape of adult neurons has remained a fundamental barrier that these factors alone cannot overcome. Our demonstration that PATZ1 can systematically reopen growth-associated enhancers provides a missing piece in the regeneration puzzle: a means to render the adult CNS epigenome receptive to pro-growth signals. This epigenetic priming strategy represents a conceptual shift from attempting to force transcription through closed chromatin to first preparing the chromatin landscape and then engaging the transcriptional machinery.

Building on this framework, future therapeutic strategies should consider combinatorial approaches that pair stripe factors like PATZ1 with pro-growth transcription factors such as KLF6, KLF7, SOX11, or NR5A2 [4,20,44–46]. PATZ1 would first establish chromatin accessibility at growth-associated enhancers, and the co-delivered transcription factors would then bind these newly available sites to drive robust transcriptional programmes. Such two-stage or simultaneous delivery strategies could produce additive or synergistic benefits that neither component achieves alone. Because AAV vectors readily target broad cortical territories, combining PATZ1 with transcription-factor cocktails, mTOR activation, or guidance-cue scaffolds is technically feasible with current vector engineering approaches.

Our curated gene list, while validated by unbiased GO-based analysis, reflects specific choices about which pathways constitute "growth-associated" programmes, and alternative selections could influence conclusions. Notably, the identification of PATZ1 as a meaningful regulator from bulk forebrain ATAC-seq data, and its subsequent validation in L5 ET neurons, suggests that broad chromatin profiling can reveal factors with cell-type-relevant functions even when derived from heterogeneous tissue. While retrograde tracing remains the definitive method for isolating corticospinal neurons specifically, our L5 ET population, enriched through anterograde labelling and marker-based identification, provides biologically meaningful data on subcortical projection neurons that include the corticospinal tract. The relationship between chromatin changes and functional axon regeneration remains to be established through tract-tracing and behavioural studies. Additionally, while our chromatin and transcriptional datasets were generated from parallel rather than single-cell multi-omic libraries, the clear convergence of accessibility, PATZ1 binding, and gene-expression changes at the same loci suggests that an integrative assay would further strengthen, rather than overturn, our conclusions.

Future work will extend these molecular findings to tract-tracing and behavioural analyses to test whether epigenetic re-opening, when combined with appropriate pro-growth factors, translates into long-distance axon growth and functional improvement. Loss-of-function studies targeting PATZ1 in the context of proximal injury would clarify whether PATZ1 is necessary for the enhanced chromatin response observed after intracortical lesions.

Taken together, these findings suggest that intrinsic regenerative failure in the adult CNS has a substantial epigenetic component that can be addressed through targeted intervention. Because PATZ1 broadens the accessibility of enhancer networks that feed into several well-established pro-growth pathways, its delivery in combination with pro-growth transcription factors, mTOR potentiators, or guidance cues could potentially be extended to spinal trauma, traumatic brain injury, and neurodegenerative settings in which dormant growth programmes must be reactivated.

**Resource availability**

All genomics datasets generated in this study have been deposited in the NCBI Gene Expression Omnibus (GEO) under accession number **PRJNA1217518**. A detailed summary of

datasets and corresponding sample information is provided in **Supplementary Table 12**. The metadata detailing the Supplementary Tables used for the results is provided in **Supplementary Table 13**. The code used for data processing and figure generation is available at https://github.com/VenkateshLab/Targeted-chromatin-remodeling-by-PATZ1.

Additionally, all datasets have been integrated into an interactive, user-friendly web interface accessible at https://patz1.netlify.app/ to facilitate data exploration.

**Acknowledgements**

We thank CSIR-CCMB for providing research facilities and support staff. We acknowledge Mrs. Zareena Begum (Tissue Culture), Mr. S. Prasanth and Mr. N. Sai Ram (Animal House), Dr. Karthik Baradwaj, Ms. Tulasi Nagabandi, and Dr. Md. Jafurulla (Genomics), Mr. G. Srinivas (FACS), and Mr. B. Suman and Dr. Nitla Venkata Mahesh (Microscopy) for their technical assistance. We also appreciate Fine BioChemical for the timely chemical supplies and Dr. Prakash Chermakani for reviewing spacing and errors in the final draft. We would also like to thank the funding agencies Council of Scientific and Industrial Research (CSIR) (HCP53201), Department of Biotechnology (DBT) (BT/PR51467/MED/122/358/2024), and Science and Engineering Research Board (SERB) (SRG00116).

**Author contributions**

ASM (Conceptualization, Data curation, Formal analysis, Investigation, Methodology, Project administration, Validation, Visualization, Writing—review & editing), MK (Data curation, Formal analysis, Software, Visualization, Writing—review & editing), DSB (Data curation, Formal analysis, Methodology, Visualisation, Writing—review & editing), DK (Formal analysis, Methodology, Visualisation, Writing—review & editing), NK (Methodology),SS (Methodology),YS (Methodology), SM (Methodology), KS (Methodology), MK (Methodology), and IV (Conceptualization, Data curation, Formal analysis, Funding acquisition, Investigation, Project administration, Resources, Supervision, Validation, Visualization, Writing).

**Declaration of Interest**

The authors declare no competing interests.

**Figure legends**

**Figure.1 ATAC-seq reveals severe restriction of promoter and enhancer accessibility in pro-growth genes across age.**

(A) Top panel: Schematic diagram of ENCODE ATAC-seq datasets isolated from the motor cortex of mice from early embryonic ages, Postnatal Day 0 (P0), and adult mouse cortex were analysed for genome-wide patterns in chromatin accessibility. Bottom panel: Representative traces of transcription factor footprinting across age. (B) Pro-growth gene-specific promoters and enhancers were isolated for further analysis based on Gene Ontology (GO) Analysis. (p-value <0.05). (C) Heatmap of promoter accessibility across ages, showing high accessibility at P0 (green) neurons and reduced accessibility in adults (red) (p-value <0.05). (D) Heatmap of enhancer accessibility across age for growth-related GO terms (p-value <0.05). (E) UCSC genome browser examples of pro-growth gene promoters with varying degrees of restriction in adults (275 total; >50% show significant restriction). (F) UCSC genome browser examples of enhancer regions with varying levels of restriction in adults (1,067 total; most show >50% restriction).

**Figure.2 Single-nuclear (sn)ATAC-seq reveals that CNS neurons mildly open the chromatin post-injury at key loci.**

(A) Schematic representation of single-nucleus ATAC-seq (snATAC) experimental workflow. (B) Uniform Manifold Approximation and Projection (UMAP) dimensional reduction plot showing single-nucleus ATAC-seq clustering. The plot displays three conditions: Uninjured (control, green), Injured (red), and Merged (combined clusters, mixed colours), along with the marker genes *Satb2, Lrp8, Etv1, Tnn1, Crym, Mrp11* marking the L5 ET clusters. (C) The bar graph (top) represents the number of chromatin accessibility peaks identified as significantly upregulated (green) and downregulated (red) post-injury in snATAC-seq analysis. Pie chart (bottom left) illustrates the genomic distribution of the upregulated peaks, with 74.4% located in potential enhancer regions and 25.6% in promoters. The histogram (bottom right) depicts the log2 fold-change distribution of upregulated peaks, with the majority exhibiting moderate fold changes. (D) Left panel bubble-plot shows clustered GO terms in two-dimensional semantic space, with circle size representing gene count and colour intensity indicating statistical significance (-log10 p-value). Right panel displays the percentage of unique injured peaks

associated with key biological processes. (E) Radar chart comparing the magnitude and distribution of chromatin accessibility changes in injured (red) neurons across six key biological pathways. The concentric circles represent Log2FC values ranging from 0.5 to 4.0. (F) Heatmap showing gene expression activity across key biological pathways as determined by GO term analysis. The vertical axis represents genes sorted by Log2FC values, while the horizontal axis displays the six major pathways. Colour intensity corresponds to Log2FC values according to the scale bar (right), with darker green indicating higher accessibility (p-value <0.05, Bonferroni correction). (G) Circular-bar plots showing the distribution of chromatin accessibility peaks based on their Log2 fold change (Log2FC) magnitudes across six key biological pathways. Each plot displays the angular position representing the magnitude of fold change (ranging from 0.5 to 5.5), which is also signified by the intensity of green shading. The radial bars indicate the number of differential accessibility peaks at each fold change value for the pathways.

**Figure.3 ATAC-seq reveals injury site proximity affects the re-opening of key loci six-fold.**

(A) Experimental workflow for ATAC-seq profiling after Intra-cortical Injury (ICI). (B) Quantification of accessible chromatin regions. Bar graph compares Thoracic crush injury (TCI) (1,390 peaks) versus ICI (13,084 peaks). Pie chart shows genomic distribution with enhancers (78.2%) and promoters (21.8%). (C) Distribution of accessible peaks by percentage fold change between injury models. ICI samples (green) show higher peak numbers with a maximum of 80-85% fold change compared to TCI samples (red). (D) Gene ontology (GO) analysis of differentially accessible regions. Dot plot shows enriched pathways with colour indicating significance (-log10(P-value)) and size showing gene count. ICI samples show greater enrichment in neuronal processes compared to TCI. (E) Pathway and gene-specific accessibility comparison. Left: Key neurobiological pathways show consistently higher accessibility in ICI versus TCI. Right: Neuronal genes (*Tubb2a, Tubb2b, Neurod2, Cux2, Chd3*) display greater accessibility in ICI than in TCI. (F) Pro-growth gene accessibility profiles. Top: Heatmap showing clustering of accessibility (green = increased). Bottom: UCSC browser tracks of six representative pro-growth genes showing higher accessibility peaks in ICI (green) versus TCI (red). (p-value <0.05). (G) Left: Schematic illustration of TF footprinting analysis showing TF binding to DNA and Tn5 transposase cleavage of accessible regions, resulting in characteristic footprint patterns. Center: Scatter plot comparing IC bound scores (x-axis) vs TC bound scores (y-axis) with marginal histograms, demonstrating differential TF binding between injury conditions. Right: Hexplot visualisation of the differences in transcription factor binding scores

between ICI and TCI conditions. The colour intensity (light to dark green) represents the magnitude of difference, with the darkest hexagons (e.g., PATZ1, SP2) indicating transcription factors with the greatest differential binding between conditions.

**Figure.4 Single-nuclear (sn)ATAC-seq reveals that chromatin around pro-growth genes becomes more accessible upon PATZ1 over-expression.**

(A) Schematic representation of single-nucleus ATAC-seq (snATAC) experimental workflow with AAV-PATZ1. (B) UMAP representation showing distinct clustering patterns between Injured control and PATZ1_Injured conditions. (C) Quantitative analysis demonstrating increased accessible chromatin regions in PATZ1 overexpression (9843) versus Injured control (5482). Pie charts displaying the genomic distribution of the PATZ1 over-expressed peaks. Histogram showing the number of accessible peaks in injured control (red) and upon PATZ1 over-expression (green). (D) Dot plot showing Top 20 Gene Ontology (GO) terms in PATZ1-overexpression versus injured control conditions. The size of dots represents the number of genes associated with each GO term, while colour intensity indicates statistical significance (-log10 p-value). (E) Circular plots comparing chromatin accessibility patterns between PATZ1-overexpressing (Blue bar) and control injured (orange bar) neurons across seven key biological pathways. Each plot displays the distribution of differential accessibility based on Log2 fold change (radial axis from 0 to 8), magnitude signified by the intensity of green shading. (F) Radar chart comparing the magnitude and distribution of chromatin accessibility changes between PATZ1-overexpressing (green) and control injured (red) neurons across seven key biological pathways. Each axis represents a distinct pathway, with the total number of associated accessible peaks indicated in parentheses. The concentric circles represent Log2FC values ranging from 0.5 to 4.0. (G) Heatmap of differential accessibility across neuronal pathways, with colour intensity representing fold change. Colour intensity (green) represents fold change in accessibility, with annotated functional pathways (p-value <0.05, Bonferroni correction, FDR <0.05). (H) Horizontal bar graph displaying the difference in Log2FC values of chromatin accessibility between PATZ1-overexpressing and injured control neurons across seven key biological pathways. The colour scale ranges from dark green (strong positive difference, indicating greater accessibility in PATZ1-overexpressing neurons) to red (negative difference, indicating reduced accessibility).

**Figure.5 Integrative analysis of single-nucleus RNA sequencing and ATAC sequencing reveals transcriptional and chromatin accessibility profiles in PATZ1 tissue sample.**

(A)Schematic illustration of the experimental workflow. (B) UMAP visualisation of single-nucleus RNA-seq (snRNA-seq) data from the PATZ1 sample. (C) Distribution of differentially expressed genes (DEGs) by fold change categories. The horizontal bar plot displays the number of upregulated (green) and downregulated (red) genes across four log2 fold-change ranges (0.5 to 1, 1 to 2, 2 to 4, and 4 and above), indicating the exact count of DEGs within each category. (D)Left: Venn diagram showing the overlap between accessible chromatin peaks identified by ATAC-seq (4483 peaks) and transcribed genes identified by RNA-seq (1131 genes), with 523 features showing both accessibility and transcription. (E) Left: Venn diagram identifying peaks accessible but not transcribed (blue), accessible with increased expression (red, 807 peaks), and closed with decreased expression (yellow, 2504 genes). (F) Heatmap showing Gene Ontology (GO) enrichment analysis of Accessible and differentially expressed genes. The left panel displays accessible and upregulated pathways (green bars), while the right panel shows accessible and downregulated pathways (red bars). Numbers within each bar indicate the count of genes associated with each biological process, and the gradient colour represents logP value from 0(light green) to 5(dark green). (G) Network visualization of gene interactions within selected biological processes. The upper panel illustrates the neuronal differentiation and nervous system development network with genes shown as nodes connected by edges representing functional interactions. The lower panel depicts the post-translational modification and nervous system development network. The gradient color scale represents the log2 fold change (logFC) values from snRNA-seq data, with green indicating upregulated genes and red indicating downregulated genes, where color intensity reflects the magnitude of differential expression.

**Figure.6 Genome-wide profiling of PATZ1 binding sites using CUT&RUN.**

(A)Schematic of the CUT&RUN workflow for mapping PATZ1 binding sites, CTCF and H3k27ac marks. (B) Genomic distribution of 5803 PATZ1-bound sites. Left: Distribution across genomic features showing Exon (3.2%), Distal Intergenic (44.6%), 5' UTR (1.8%), Intron (36.8%), and Downstream (<300bp) (9.1%). Right: Regulatory element classification showing Potential Enhancers (86.2%), Promoters (13.8%), and TTS (0.1%).(C) Genome browser tracks showing PATZ1-induced chromatin accessibility at pro-growth genes. Left panel: Representative loci (Klf7, Satb3, Sox11) showing increased chromatin accessibility in PATZ1-injured (green) compared to injured control (blue). Right panel: Additional loci (Sgo1, Rarg, Sh1sa2) with enhanced accessibility. Yellow bars indicate proximal or distal enhancers; blue boxes mark CTCF binding sites. Black arrows indicate genomic distances and enhancer locations

relative to gene bodies.(D) Detailed view of PATZ1 binding, CTCF occupancy, and H3K27ac marks at the Cux2 locus. Tracks show Injured_CTCF (red), Injured_H3K27me (red), Injured control (red), PATZ1_Injured_CTCF (green), PATZ1_Injured_H3K27me (green), and PATZ1_Injured (green). Yellow bars indicate proximal enhancer and H3K27me regions. (E) Distribution and characterization of PATZ1 binding at cis-regulatory elements. Left: Percentage distribution showing distal enhancer-like (dELS, 36.60%), CTCF-only (23.03%), proximal enhancer-like (pELS, 22.55%), promoter-like (PLS, 13.89%), and DNase-H3K4me3 (3.83%). Right: CTCF motif enrichment relative to PATZ1 binding sites categorized by binding strength (Far: pink, >100kb; Medium: green, 50kb; Near: orange, <10kb), with count distribution shown on x-axis.(F) Overlap of H3K27ac-enriched regions between injured (246 unique) and PATZ1-treated injured samples (2847 unique), with 888 shared regions. Right: Browser views showing PATZ1-dependent H3K27ac enrichment (blue) compared to injured-only samples (yellow). (G) GO analysis of H3K27ac regions unique to PATZ1-treated injured samples. (H) Regeneration-associated pathways enriched in H3K27ac-marked regions: gained (green) and lost (red) in PATZ1-treated injured samples. (I) Overlap of CTCF binding sites between injured (1506 unique) and PATZ1-treated injured (1026 unique) samples, with 923 shared sites. Right: Browser tracks showing condition-specific CTCF peaks. (J) GO analysis showing pathways with CTCF lost (pink) and gained (green) between conditions. Dot size: gene count; colour intensity: significance (-log10(p-value).

**Figure.7 Functional analysis of compartment switching by PATZ1**

(A)Experimental workflow for Hi-C analysis. (B) Genome browser tracks at axon growth genes (Tubb2a, Sgo1, Icam1) comparing PATZ1-injured (green) versus injured control (red) samples. Tracks show 3D chromatin organization with TAD boundaries (top), CTCF binding, active enhancer/promoter marks (H3K27ac), regulatory factor binding, chromatin accessibility (ATAC-seq), and transcriptional activity. Loops indicate chromatin interactions between regulatory elements. Gene structures shown below with exons as blue boxes.(C) Top: Depicts a model of nuclear organisation showing A/B compartmentalisation (green/red) and compartment shifts between conditions. Bottom: The bottom scatterplot shows principal component analysis of genomic regions, with points coloured by compartment switching status: B→A regions (3557 regions, 3.5% of total) in green, A→B regions (2949 regions, 2.9%) in red, and non-switching regions in gray. The x-axis shows principal component (PC) values of the injured condition, while the y-axis shows principal component (PC) values of the PATZ1 condition. (D)

Hierarchical representation of the top 10 Gene Ontology (GO) terms enriched in B→A compartment switches (left, green) and A→B compartment switches (right, red). Colour intensity indicates gene count ($p<0.05$). (G) Quantification of Topologically Associating Domains (TADs) across categories showing conserved (1319), Injured-unique (1052), PATZ1-unique (2500) and shifted (2602). (H) Distribution comparisons between Injured (red) and PATZ1 (green) conditions: IR values(left), TAD lengths (middle), and Log2FC read counts (right).

**Supplemental information**

**Document S1. Figures S1–S15,**

**Supplementary Table S1**: Excel file containing data that is used to generate Figure 1

**Supplementary Table S3**: Excel file containing data that is used to generate Figure 2

**Supplementary Table S4**: Excel file containing data that is used to generate Figure 3

**Supplementary Table S6**: Excel file containing data that is used to generate Figure 4

**Supplementary Table S7**: Excel file containing data that is used to generate Figure 5

**Supplementary Table S9**: Excel file containing data that is used to generate Figure 6

**Supplementary Table S10**: Excel file containing data that is used to generate Figure 7

**Supplementary Table S2**: Excel file containing data that is used to generate Supplementary Figure S 2

**Supplementary Table S5**: Excel file containing data that is used to generate Supplementary Figure S 7

**Supplementary Table S8**: Excel file containing data that is used to generate Supplementary Figure S 10

**Supplementary Table S11**: Excel file containing data that is used to generate Supplementary Figure SF 15

**Supplementary Table S12**: A detailed summary of datasets and corresponding sample information

**Supplementary Table S13**: The metadata detailing the Supplementary Tables used for the results

## Materials and Methods

### Animal Husbandry

All experimental protocols involving animals were approved by the Institutional Animal Ethics Committee (IAEC) of the Centre for Cellular and Molecular Biology (CCMB), Hyderabad, India (IAEC 14/2023, 29/2023, 51/2023, 10/2024, 53/2024). Mice (C57BL/6J strain) were bred and maintained under a 24-hour light-dark cycle with 12 hours of light and 12 hours of darkness. The ambient temperature was maintained between 23-25°C with humidity levels between 40% and 60%.

### Cloning and Virus Production

Constructs for candidate genes were purchased from Horizon Discovery: pCMV-SPORT6-PATZ1 (Clone ID: 4167023) from the MGC Fully Sequenced Mouse cDNA (pCMV) Set Transcription Factors (Catalog ID: MMM5173, Expression Ready MGC cDNA Libraries), while pAAV-CAG-tdTomato (codon diversified) and pAAV-CAG-GFP were purchased from Addgene (Plasmid catalogue ID# 59462, #37825). For viral production, the ORF of each gene was cloned into an AAV-CAG backbone (Addgene Plasmid #59462) using a standard cut-and-paste method. Maxipreps were prepared (Qiagen Endo-free kits, #1236) and fully sequenced. AAV9-tdTomato (Addgene Plasmid #59462) was produced in-house, achieving a titer value of 10×10^11 to 10^13 before injection. For experiments, viruses were mixed at a 1:3 ratio of pAAV-CAG-GFP to pAAV-CAG-PATZ1. If using KLF6, mention the catalogue number

### Animal Surgeries

### Anterograde Injections

Following deep anaesthesia with ketamine (100mg/ml)/Xylazine (20mg/ml), mice were prepared by shaving and disinfecting the scalp and neck. They were positioned in a stereotaxic frame, and a 1 cm midline incision was made in the scalp. The skin was retracted using a Bulldog clamp, and a thin layer of the skull was gently peeled away. Non-replicating viral particles were injected using a Hamilton syringe (Sigma Aldrich, #20972) at four bilateral points relative to Bregma, with coordinates (x = -2, +2; y = -0.5, +0.5, z= 0.8, 0.6), delivering

1 µl of AAV (0.2 µl/2 min) to ensure widespread diffusion. After withdrawing the pipette, the incision was sutured, and appropriate postoperative care was administered.

**Thoracic Crush**

Mice (n=3) post seven days of injection, were anaesthetised with ketamine (100mg/ml)/Xylazine(20mg/ml) and prepared for surgery by shaving and disinfecting the upper back and neck. A midline incision was made from the ears to approximately 2 cm down the neck and back. Fatty tissue was displaced laterally, and a bulldog clamp was used to retract skin and maintain exposure of the surgical site. The underlying paraspinal musculature was carefully dissected to expose the spinal column. The spinous processes at the T10-T12 level were identified and trimmed, if necessary, to facilitate access. The mouse was then mounted in a custom spine stabiliser to ensure proper immobilisation during the procedure. A laminectomy was performed at the T10-T12 level using fine forceps to carefully remove the dorsal lamina and expose the spinal cord. The exposed spinal cord was then crushed with calibrated blunt forceps for a precise duration of 10 seconds, applying consistent pressure across the full width of the cord. Following a crush injury, the vertebral column was repositioned, the surrounding tissues were returned to their anatomical positions, and the skin was sutured with black nylon thread. Post-operative care included analgesics, antibiotics, manual bladder expression twice daily until function returned, and maintenance on a heating pad during recovery. Visible hindlimb paralysis was consistently observed post-surgery, confirming successful injury. All procedures were performed in a type II safety hood under aseptic conditions.

**Intra-cortical Surgery**

This procedure was modified from Wang *et al*., 2025 [6]. After deep anaesthesia with ketamine (100mg/ml)/Xylazine (20mg/ml), mice (n=3) were prepared by shaving the scalp and neck and disinfecting with betadine. Mice were positioned in a stereotaxic frame, and a 1 cm midline incision was made in the scalp. The skin was retracted with a Bulldog clamp, and the skull over the injection area was gently peeled away. Stereotaxic coordinates (x = -2, y = -0.5, y = +0.5, z = 0.6) were used to guide the procedure at specified points. A 30½ gauge needle bent into an L-shape was inserted 0.6 mm from the brain surface and turned 90 degrees to sever axons. The needle was retracted, the skin was sutured, and post-operative care was provided.

**Pyramidotomy**

The procedure was adapted from [47]. Seven days post-injection, deep anaesthesia with ketamine (100mg/ml)/Xylazine (20mg/ml) was administered to mice (n=3 for control and n=4 for PATZ1 treated animals). A ventral incision was made near the oesophageal region, and after displacing the tissue layer beneath with blunt forceps, the medullary pyramid was exposed. The dura was cut, and the right pyramidal tract was incised using iridectomy scissors (0.5 mm width, 0.25 mm depth). Post-surgery, the oesophagus, trachea, and muscles were repositioned, and the skin was sutured.

**Axon-growth quantification for Pyramidotomy cord slices**

Tissue preparation and imaging: At 8 weeks post-pyramidotomy, animals were transcardially perfused and spinal cords were processed as described below. For each animal, six transverse sections (50 µm thickness) spanning the C2-C4 spinal cord segments (1.5 mm spacing between sections) were selected for analysis. Sections were imaged using a Leica STED/confocal microscope with a 63× objective (tile scan in 520 × 520 µm format, 0.5-1 µm z-steps, scan speed 400 Hz; detector gain 1,250 V, laser power 40%). Maximum intensity projections were generated from the z-stacks for quantification.

**Fibre index calculation**: Axonal regeneration was quantified by calculating a Fiber Index (FI) based on the number of GFP-positive axons crossing predefined virtual distance bins distal to the lesion. For each spinal cord section, the midline border was first identified anatomically using the spinal canal as a reference. A reference line was then drawn through the central canal at the lesion epicenter (0 µm) to establish the point of origin for subsequent measurements. Automated quantification was performed using DeNAT, a machine-learning–based tool for neurite detection and spatial measurement [48]. After uploading each GFP-labeled spinal cord image, users manually defined (i) the midline and (ii) the region of interest (ROI) corresponding to the injured and regenerating side. Based on the image's spatial calibration and pixel-to-micron ratio, DeNAT automatically generated four parallel virtual lines caudal to the lesion border at the following distances: 0–200 µm, 200–400 µm, 400–600 µm and >600 µm. The integrated ML model then detected GFP-positive fibers and quantified the number of axons crossing each virtual line. The Fiber Index for each distance bin was calculated as the number of GFP-positive axons was normalized based on each bins.

To normalize for variability in viral transduction efficiency, GFP-positive neurons in the medullary pyramids were quantified. Coronal sections (50 µm) through the medullary pyramids were imaged (3-4 slices per) animal) using a Zeiss ApoTome microscope at 10× magnification. GFP-positive cell bodies were counted from 3-4 sections per animal using ImageJ software [49]. The fiber index for each distance bin was calculated by dividing the average number of axons crossing each distance line by the normalized pyramid cell count, providing a measure of axonal density that accounts for differences in initial labeling efficiency between animals.

**Statistical analysis**: Fiber index data were analyzed using two-way ANOVA between control and treated fibre indices(AAV-GFP vs. AAV-PATZ1) and distance from the lesion (0-200 µm, 200-400 µm, 400-600 µm, >600 µm) as fixed factors, and subject as a random effect to account for repeated measurements across distances within individual animals. This measures both main effects and the treatment × distance interaction term. Post-hoc pairwise comparisons between treatment groups at each distance were performed using Sidak's multiple comparisons test to control for family-wise error rate. Data are presented as mean ± SEM with n = 3-4 animals per group. Statistical significance was set at $\alpha = 0.05$. All statistical analyses were performed using GraphPad Prism version 10.5.0 (GraphPad Prism Software, Boston, Massachusetts USA, www.graphpad.com)

**Immunohistochemistry**

For spinal injury experiments, adult animals were decapitated following anaesthesia, and the brain and spinal cord were extracted and post-fixed overnight in 4% PFA (Sigma Aldrich, #158127) at 4°C. Spinal cord tissue was embedded in 12% gelatin (Sigma Aldrich, G2500) in PBS, and 50 µm sagittal sections were obtained using a vibratome. Sections were permeabilised in PBST, blocked with 5% normal goat serum, and incubated overnight at 4°C with the following primary antibodies: anti-GFAP (Cell Signalling Technology, mAb #3670, 1:500) to assess injury depth; PKCγ (GeneTex, GTX107639, 1:200) to confirm unilateral pyramidotomy; CTCF (Cell Signalling Technology, #3418, 1:500) and H3K27ac (Abcam, ab4729, 1:500) for antibody validation; and PATZ1 (MyBioSource, MSB9403528, 1:100) to confirm PATZ1 overexpression. After three PBS washes, sections were incubated with Alexa Fluor-conjugated secondary antibodies (Thermo Fisher, R37119, 1:500) for 2 hours at room temperature. Following counterstaining with DAPI (F6057-Sigma Aldrich), sections were mounted and imaged using a confocal microscope for high-resolution analysis.

**Nuclear extraction and Fluorescence-activated nuclei sorting (FANS)**

Adult mice (n=3 per experimental group) received anterograde injections of viral vectors for Control and PATZ1 treatment. One week later, animals were challenged with thoracic crush injuries, as described above. One week post-injury, animals were sacrificed, and the motor cortices were dissected. Tissue was collected only from the motor cortex region, which shows green fluorescence under UV light when viewed through a yellow filter. The dissected motor cortex tissues were added to pre-chilled 2 ml EZ lysis buffer (Sigma, NUC-101) and dounced (Sigma, D8938) slowly and carefully (Dounce A, 40 times; Dounce B, 45 times), then incubated for 5 minutes at room temperature. Post incubation, the content was transferred to a 15ml falcon tube and centrifuged at 500g with acceleration and deceleration set to 2. The supernatant was removed, and the pellet was dissolved in Nuclear Suspension Buffer (freshly prepared: 5 mL PBS, 25 uL BSA (20 mg/mL) and 25 uL RNase inhibitor (40 U/uL) (Invitrogen, 10777019)) and strained through a Polystyrene tube with cell strainer (Falcon, 352235). Dissociated nuclei were flow-sorted on a BD FACS using an appropriate gating strategy (Sort type: Purity). Nuclei were first gated by side scatter height (SSC-H) vs. forward scatter height (FSC-H) and side scatter area (SSC-A) vs. FSC-A to separate debris from intact nuclei. Nuclei that passed these filters were further selected by SSC-W vs. SSC-H to eliminate potential doublets. Finally, nuclei were gated by fluorescence marker intensity to collect only the brightest approximately 5000 nuclei for ATAC sequencing.

**Single-Nucleus ATAC Sequencing Library construction (sn-ATAC)**

Single-cell ATAC-seq datasets were generated using the Chromium Single Cell ATAC kit from 10x Genomics, following the manufacturer's instructions (10x Genomics, CG000496 Chromium Next GEM Single Cell ATAC Reagent Kit v2). Nuclei were isolated from the motor cortex of mice (n=3 per experimental group). The isolated nuclei suspensions (3,000-5,000 nuclei per sample) were added to the transposition mix containing Tn5 transposase enzyme, which simultaneously fragments DNA and inserts adapter sequences at accessible chromatin regions. Gel beads in emulsion (GEMs) were generated on the Chromium Next GEM Chip H by combining barcoded gel beads with the transposed nuclei suspension and partitioning oil. After GEM generation, the barcoded DNA fragments were recovered and purified using streptavidin beads, followed by size selection with SPRIselect beads (Beckman Coulter,

B23318) and a series of 80% ethanol washes. The purified DNA fragments were eluted in elution buffer (10 mM Tris-HCl pH 8.0), followed by indexing PCR amplification (12 cycles) to add sample indices and Illumina sequencing adapters. Final library cleanup was performed using an additional round of size selection with SPRIselect beads. Library quality was assessed using a Bioanalyzer High Sensitivity DNA Kit (Agilent, 5067-4626) to confirm appropriate fragment size distribution (200-800 bp). Sequencing was performed on an Illumina NovaSeq 6000 instrument using a paired-end configuration with read length of 2X150 bp, approximately 300 million paired-end reads per sample to achieve sufficient coverage for downstream analysis.

**Bulk Assay for Transposase-Accessible Chromatin Sequencing (Bulk ATAC)**

Motor cortices were isolated from mouse pups at P0, P4, P7, and from adult mice (n=3 per experimental group) that underwent intra-cortical and thoracic crush surgery. Tissue samples (20-30 mg) were minced and placed into ice-cold PBS. Nuclei extraction was performed following the protocol described above. Nuclei were counted, and approximately 50,000 to 100,000 nuclei per sample were used for the assay. The nuclear pellet was resuspended in Tagmentation Master Mix containing transposase enzyme (Active Motif, #53150), which inserts sequencing adapters into accessible regions of chromatin according to the manufacturer's protocol. Tagmentation was carried out by incubating the nuclei with the Tagmentation Master Mix at 37°C for 30 minutes with gentle agitation. Following tagmentation, the DNA was purified using a DNA purification column (Active Motif, included in kit). The purified DNA was eluted in 10 mM Tris-HCl (pH 8.0) and subjected to PCR amplification (12-15 cycles) using indexed primers compatible with Illumina sequencing. Post-PCR, a final purification step was performed using SPRI beads (Beckman Coulter, B23318) at a 1.8× ratio to remove primer dimers and unincorporated primers. Libraries were quantified using Qubit dsDNA HS Assay Kit (Thermo Fisher, Q32851), and DNA size distribution was assessed with a TapeStation 4200 (Agilent) using a D1000 ScreenTape (Agilent, 5067-5582) before pooling and loading the libraries onto the Illumina NovaSeq 6000 sequencing platform for ~30 million paired-end reads per library.

**High-throughput Chromosome Confirmation Capture (Hi-C)**

Mice (n=3 to 4 per experimental group) used for the assay were subjected to anterograde injections of AAV9-PATZ1, followed by a thoracic crush injury one week later.

Hi-C was performed on two types of tissues: mice at 7 days post-injury, and injured mice injected with AAV9-PATZ1, with the protocol individually performed for each tissue type. Hi-C was carried out following the in situ Hi-C protocol provided by the ENCODE Consortium. Briefly, the motor cortices (35-40mg, from 3 to 5 animals) were isolated from the mouse brain, and the tissues were crosslinked with 1% formaldehyde (Thermofisher, 12755) for 10 minutes at room temperature. After quenching with 2.5M glycine solution (MP Biomedicals, 808822) to a final concentration of 0.2M for 5 minutes, nuclei were isolated through cell lysis using cold Hi-C lysis buffer (5mM CaCl2, 3mM MgAc, 2mM EDTA, 0.5mM EGTA, 10mM Tris-HCl pH8.0, 1mM DTT, 0.1mM PMSF) with protease inhibitors (MCE, HY-K0010). After density gradient centrifugation with 1M Sucrose solution, nuclei were resuspended in 0.5% SDS and incubated at 62°C for 10 minutes. SDS was quenched with 10% Triton X-100, and chromatin was digested with 100U of MboI restriction enzyme (NEB, R0147) at 37°C overnight. Following enzyme inactivation at 62°C for 20 minutes, DNA ends were filled in with a mix containing biotin-14-dATP (0.4mM) (Thermo Scientific, 19524-016), dCTP, dGTP, dTTP (10mM each) (Thermo Scientific, 18254011, 18253013, 18255018) and DNA Polymerase I Klenow Fragment (NEB, M0210) at 37°C for 45 minutes. Ligation was performed in a master mix containing T4 DNA ligase buffer, 10% Triton X-100, 20mg/ml BSA (Catalog no : A7906-Sigma), and T4 DNA Ligase (NEB, M0202) at room temperature for 4 hours. After proteinase K (Sigma, P2308) treatment and crosslink reversal at 65°C overnight, DNA was purified, sheared using Covaris (M220, Condition Peak Incident: 50, Duty Factor= 10, Cycles/Burst=350, Treatment Time= 70), and size-selected for 300-500bp fragments using AMPure XP beads (Beckman Coulter, A63881). Biotin-labeled fragments were captured with Streptavidin T1 beads (Invitrogen, 65601), end-repaired, dA-tailed, and ligated to Illumina adapters (Illumina TruSeq UD Indexes, 20040870). The final library was PCR amplified (Illumina, 20015964), purified again with AMPure XP beads, and sequenced to a depth of ~500 million paired-end reads on the Illumina NovaSeq 6000 platform.

**Cleavage Under Targets and Release Using Nuclease Sequencing (CUT&RUN)**

Mice (n=3 per experimental group) received anterograde intracortical injections of AAV9-PATZ1, followed by thoracic spinal cord injury seven days later. CUT&RUN was performed using the DNA-Protein Interaction Assay Kit (Cell Signalling Technology, #86652) according to the manufacturer's protocol. Motor cortices were dissected and fixed with 0.1% formaldehyde (Cell Signalling Technology, #12606P), then quenched using 10x glycine (Cell

Signalling Technology, #7005S). Tissue was dissociated into cell suspensions using a Dounce homogenizer (Sigma, D8938) in wash buffer containing spermidine (Cell Signalling Technology, #27287) and protease inhibitors (Cell Signalling Technology, #7012). Cells were bound to activated Concanavalin A beads and incubated overnight at 4°C with the PATZ1 antibody (MyBioSource, MSB9403528).

The following day, pAG-MNase enzyme was added in a buffer premix (Cell Signalling Technology, #15338) containing digitonin (Cell Signalling Technology, #16359), spermidine, and protease inhibitors, and incubated with the sample for 1 hour. DNA cleavage was activated on ice by adding $CaCl_2$ in a digitonin-containing buffer and incubating at 4°C for 30 minutes. DNA fragments were released by adding Stop Buffer (Cell Signalling Technology, #48105) containing digitonin and RNase A (Cell Signalling Technology, #7013), followed by a 10-minute incubation at 37°C. Crosslinks were reversed using 10% SDS and 20 mg/mL Proteinase K (Cell Signalling Technology, #10012), with incubation at 65°C for 2 hours. DNA was purified using DNA Purification Buffers and Spin Columns (Cell Signalling Technology, #14209) following the manufacturer's recommended protocol. Libraries were prepared by end repair, adaptor ligation, and PCR amplification using the NEBNext® Ultra™ II DNA Library Prep Kit (NEB, #E7103).

Input samples were prepared using a similar protocol, except they were not treated with antibody or pAG-MNase. Instead, DNA was extracted using DNA Extraction Buffer (Cell Signalling Technology, #42015) for sonication (Covaris M220; 100–600 bp, Peak Incident: 75, Duty: 10, Cycles/Burst: 200, 75 s), followed by library preparation. Both CUT&RUN and input libraries were sequenced to 5 million paired-end reads (Illumina NovaSeq 6000).

Additionally, motor cortices were isolated from uninjured mice, mice 7 days post-injury, and mice treated with AAV-PATZ1 prior to thoracic injury. CUT&RUN assays were performed using the H3K27ac antibody (Abcam, ab4729) and CTCF antibody (Cell Signalling Technology, #3418), following the manufacturer's protocol outlined above. These libraries were then amplified and sequenced to a depth of 5 million paired-end reads.

**Single-nuclei RNA Sequencing**

Single-nuclei RNA sequencing (snRNA-seq) was performed using the Chromium Next GEM Single Cell 3' v3.1 (Dual Index) platform (10x Genomics) following the manufacturer's protocol (Document CG000315 Rev F). Nuclei were isolated from the motor cortex of mice

(n=3 per experimental group) injected with AAV-GFP (control) and AAV-PATZ1 according to the nuclei isolation procedure mentioned above. It was then FACS sorted to isolate only GFP and DAPI (F6057-Sigma Aldrich) positive nuclei population. The cell suspensions were loaded onto the Chromium Next GEM Chip G (PN-2000177) for generating Gel Beads-in-Emulsion (GEM). Single cell suspensions were combined with Master Mix containing RT Reagent B (PN-2000165), Template Switch Oligo (PN-3000228), Reducing Agent B (PN-2000087), and RT Enzyme C (PN-2000085/2000102). A total of approximately 4000 cells were targeted. Cell suspensions and Master Mix were loaded into the Chromium Next GEM Chip G along with Single Cell 3' v3.1 Gel Beads (PN-2000164) and Partitioning Oil (PN-2000190).

The chip was processed on the Chromium Controller to generate GEMs. Within each GEM, cells were lysed, and mRNAs were captured by poly(dT) oligonucleotides attached to the gel beads, which also contained a 16-nucleotide 10x Barcode, a 12-nucleotide Unique Molecular Identifier (UMI), and adaptor sequences. Reverse transcription was performed within the GEMs using the following thermal cycling protocol: 53°C for 45 minutes, followed by 85°C for 5 minutes. Following reverse transcription, GEMs were broken using Recovery Agent (PN-220016), and the barcoded, full-length cDNA was purified using Dynabeads MyOne SILANE (PN-2000048). Cleanup Buffer (PN-2000088) and Reducing Agent B (PN-2000087) were used in the Dynabeads Cleanup Mix. The purified cDNA was amplified using cDNA Primers (PN-2000089) and Amp Mix (PN-2000047/2000103) with the following cycling parameters mentioned in the protocol. The number of PCR cycles was optimised based on the targeted cell recovery, with 12 cycles used for 500-6,000 cells. Amplified cDNA was cleaned up using SPRIselect reagent (Beckman Coulter, PN B23318) at a ratio of 0.6X, and the purified cDNA was quality-checked and quantified using the Agilent Tapestation 4200 using D1000 tape (PN-5067-5586). All data are hosted at https://patz1.netlify.app/ for easy access.

For library construction, 25% of the total cDNA yield was used as input. The cDNA was enzymatically fragmented using Fragmentation Enzyme (PN-2000090/2000104) and Fragmentation Buffer (PN-2000091), followed by end-repair and A-tailing. The fragmentation reaction was incubated at 32°C for 5 minutes, followed by 65°C for 30 minutes. Size selection was performed using SPRIselect reagent with a double-sided protocol (0.6x followed by 0.8x) to obtain fragments of optimal size. Adaptor ligation was performed using Ligation Buffer (PN-2000092), DNA Ligase (PN-220110/220131), and Adaptor Oligos (PN-2000094) at 20°C

for 15 minutes. After another round of cleanup using SPRIselect (0.8x), Sample Index PCR was performed using Amp Mix (PN-2000047/2000103) and dual indices from the Dual Index Kit TT Set A (PN-1000215, containing index plate PN-3000431). PCR cycling conditions were: 98°C for 45 seconds, followed by 12 cycles of (98°C for 20 seconds, 54°C for 30 seconds, 72°C for 20 seconds), with a final extension at 72°C for 1 minute. The final libraries were purified using a double-sided size selection with SPRIselect (0.6x followed by 0.8x) to remove adapter dimers and were eluted in Buffer EB (Qiagen, PN-19086).

Libraries were quality-checked using an Agilent Tapestation with D1000 tape to verify fragment size distribution (~200-2,000 bp with a peak around 400 bp). Libraries were sequenced on an Illumina NovaSeq 6000 sequencer with a depth of 300 million paired-end reads.

**Adeno-Associated Virus Production**

Adeno-associated viral (AAV) particles, serotype 9, were packaged and produced in HEK293T cells and then purified using a commercial AAV purification kit (Takara, #6666). Briefly, HEK293T cells were transiently transfected with pAAV-CAG-Patz1, pAAV2/9n (Addgene, #112865), and pAdDeltaF6 (Addgene, #112867) using Transfection Grade Linear Polyethylenimine Hydrochloride (MW 40,000) (Polysciences, #24765). At 48 hours post-transfection, cells were dislodged and transferred to sterile 50 ml falcon tubes. Viral isolation (Takara, #6666) was performed following the manufacturer's instructions. To assess AAV capsid formation, proteins were separated on a 10% SDS-PAGE gel at 35 mA for 120 minutes. The gel was stained with Coomassie Brilliant Blue (Himedia, #17524.02) for 20 minutes, followed by overnight destaining in a solution of 10% acetic acid (Himedia, #90868) and 40% methanol (Himedia, #AS059) in water. SDS-PAGE analysis confirmed the presence of all three AAV capsid proteins: VP1 (83kDa), VP2 (73kDa), and VP3 (62kDa), with VP3 being the most abundant, as expected for correctly assembled AAV particles. For viral titer quantification, qPCR was performed using the Takara TB Green Premix Ex Taq II kit (Takara, #RR82WR). Viral particles were first treated with DNase for 30 minutes at 37°C, then serially diluted ten-fold across four dilutions. The viral titer was estimated by comparing the Ct values of the viral particles with a known plasmid standard (Addgene Plasmid, #59462) from a standard curve. All AAV preparations yielded titers of 10^11 viral genomes per ml or higher, with intact capsid formation confirmed by SDS-PAGE analysis.

## Single Nuclear ATAC Sequencing Analysis Pipeline

Cell Ranger ATAC version 7.2 was used to process Chromium scATAC-seq data following protocols described previously [50]. Fragment files were imported into ArchR version 1.0.2 [51]. We applied stringent quality control filters, retaining only cells with >1,000 fragments and >4 transcription start site (TSS) enrichment score. After quality control and filtering of empty droplets and doublets, we identified approximately 72,000 peaks from 1,500 nuclei per sample. Gene activities for each nucleus were calculated using the GeneScoreMatrix() function by summing peak counts in the gene body plus 2 kilobase pairs (kb) upstream[51]. Data were normalized using term frequency-inverse document frequency (TF-IDF) normalization (RunTFIDF), followed by dimensionality reduction using singular value decomposition (RunSVD). K-nearest neighbors were calculated using FindNeighbours (reduction = "lsi", dims = 2:30). Cell clusters were identified using a shared nearest neighbor (SNN) modularity optimization-based clustering algorithm FindClusters (algorithm = 3, resolution = 2). UMAP visualization was generated using the RunUMAP function with reduction = "lsi" and dims = 2:30. Peaks were called using the addReproduciblePeakSet() function in ArchR using the Tiles matrix method with a fixed width of 501 base pairs. The complete automated analysis workflow is documented in detail on our GitHub repository https://github.com/VenkateshLab/Targeted-chromatin-remodeling-by-PATZ1. We utilised in R shiny app to provide pre-built clusters of the analyzed snATAC-seq data, enabling direct visualization and interactive exploration. The clustered data is publicly accessible through our website (https://patz1.netlify.app/).

## Bulk ATAC Sequencing Analysis Pipeline

Mouse forebrain samples were collected from the ENCODE[37] and in-house data sets (P4 and P7) project at various developmental stages, including embryonic days E11 (ENCSR273UFV), E12 (ENCSR559FAJ), E13 (ENCSR903GMO), E14 (ENCSR810HQR), and E18 (ENCSR836PUC), as well as postnatal stages P0 (ENCSR310MLB), P4, P7 and adult (P36) (ENCSR976LWP). Additional Bulk ATAC-seq datasets were generated for other developmental stages as described above. Paired-end reads were trimmed using fastp to remove adapter sequences and low-quality bases [52]. Trimmed reads were aligned to the mouse genome (mm10) using the STAR version 2.7.11a aligner with default parameters [53]. We filtered out reads with mapping quality scores lower than 10 using SAMtools version 1.19 and removed duplicate reads using the MarkDuplicates function from the Picard toolkit [54]. For downstream analysis, we employed the TOBIAS-snake pipeline with default parameters [55]. BigWig files

were generated for visualization in the UCSC Genome Browser [56]. The complete automated pipeline details are available in our GitHub repository https://github.com/VenkateshLab/Targeted-chromatin-remodeling-by-PATZ1.Furthermore, the bed files from Embryonic, Postnatal, and Adult stages were used for Transcription Factor Co-Occurrence analysis using TF-COMB[57].

**Batch Correction**

We modeled batch effects directly on per-sample read counts obtained from the E11–E18, P0, P4, P7, and Adult BAM files. A negative binomial regression framework was used to fit batch-specific effects while retaining developmental stage as the biological factor. The observed counts were then mapped to their expected values under the no-batch-effect distribution to obtain adjusted BAM-derived expression matrices. Finally, PCA was performed on both the raw and adjusted matrices to assess the success of the correction. The first principal component accounted for 29.49% of the variance prior to correction and 31.56% after correction.

**CUT&RUN Analysis Pipeline**

Raw sequencing reads were processed with FastP for adapter removal and low-quality read trimming. Clean reads were aligned to the mouse genome (mm10) using BWA-mem version 0.7.19 with default parameters [58]. Aligned reads were converted to BAM format and sorted using SAMtools, and PCR duplicates were removed with Picard. Peak calling was performed using MACS2 with default parameters[59]. Identified peaks were annotated using GenomicRanges and ChIPseeker packages in R version 4.4.2 [60]. The annotated BED files were further analyzed to identify CTCF binding sites and enhancer regions using resources from the SCREEN project from ENCODE[37]. The complete automated analysis workflow is documented in detail on our GitHub repository mentioned above.

**snRNA-seq Data Analysis Pipeline**

Our workflow began with raw data quality assessment using FastQC ensuring sequencing data met basic quality thresholds for base quality, adapter contamination, and overall read quality. Following quality assessment, we used FastP to remove low-quality reads, filtering out those with poor quality scores or excessive adapter sequences [52]. The cleaned data was processed using CellRanger, which was specifically designed for single-nucleus RNA-seq

data alignment and quantification [61]. We used the mm10 mouse reference genome with default parameters to generate high-quality alignments. Samples were sequenced to an average depth of ~70,000 reads/nucleus (3,000-4,000 nuclei per library) on an Illumina NovaSeq 6000 platform.

The datasets were integrated using SEURAT v5 [62] and differential expression analysis was conducted using the "FindMarkers" function, applying a nonparametric Wilcoxon rank-sum test. Cluster visualization in Seurat was generated using the "scCustomize" package in R (https://github.com/samuel-marsh/scCustomize), while MA-plots, histograms, and heatmaps were created using the "ggplot2" package (https://ggplot2.tidyverse.org/). We utilised ShinyCell in R to provide pre-built clusters of the analyzed scRNA-seq data, enabling direct visualization and interactive exploration [63]. The clustered data is publicly accessible through our dedicated (https://patz1.netlify.app/).

**Hi-C Data Processing and 3D Genome Architecture Analysis**

Paired-end Hi-C sequencing reads were initially subjected to quality control using FastQC (v0.11.9)[64] to assess base quality, GC content, and adapter contamination using FastP (v0.23.3)[52] . Trimming of 3′ overhangs was performed using homerTools (v4.11), specifically targeting the MboI/DpnII restriction enzyme motif (GATC), with parameters -mis 0, -matchStart 20, and -min 20. Both R1 and R2 reads were trimmed independently, as paired-end alignment is not recommended for HOMER Hi-C analysis.Trimmed reads were aligned to the Mus musculus mm10 reference genome using Bowtie2 (v2.5.1) with the -U flag for unpaired alignment and -p 30 for parallel processing[65]. The resulting SAM files were used to generate a Hi-C tag directory via HOMER's makeTagDirectory function, using the -tbp 1 option to remove PCR duplicates. Additional QC metrics were generated using parameters such as -checkGC, -restrictionSite GATC, and -genome mm10. For interactive visualization in Juicebox, .hic files were generated using HOMER's tagDir2hicFile.pl utility [67].

**Chromatin Compartment Analysis (PCA)**

Principal component analysis (PCA) was performed using the runHiCpca.pl script to identify chromatin compartments (A/B) at a resolution of 25 kb with a 50 kb smoothing window. This analysis generated both .PC1.bedGraph and .PC1.txt files, where the PC1 values correlate with open (A) and closed (B) chromatin domains. The bedGraph files were visualized in a genome browser and used for comparative analysis between control and treated samples.

Control vs. treated conditions were integrated using annotatePeaks.pl, and differentially enriched compartments were identified using getDiffExpression.pl, with group labels specified according to replicate structure.

**Chromatin Compaction Analysis**

Chromatin compaction was quantified using distal-to-local interaction ratios (DLR) and interchromosomal interaction fractions (ICF) via the analyzeHiC function with -compactionStats parameter. This analysis was performed at 5 kb resolution with a 15 kb window. Output .DLR.bedGraph and .ICF.bedGraph files were processed using subtractBedGraphs.pl to identify differential compaction profiles across conditions.

**TAD and Loop Detection**

Topologically associating domains (TADs) and chromatin loops were detected using findTADsAndLoops.pl with a 3 kb resolution and a 15 kb window size. The resulting .loop.2D.bed and .tad.2D.bed files were visualized using Juicebox [66] and served as the basis for cross-condition comparisons. To compare loop and TAD dynamics between control and treated samples, feature files were first merged using merge2Dbed.pl. Quantification was performed using findTADsAndLoops.pl score across all tag directories. Differential enrichment analysis was conducted using getDiffExpression.pl, identifying significantly altered loops and TADs between conditions via an edgeR-based statistical framework [68].

**References**


1. Sun, F., and He, Z. (2010). Neuronal intrinsic barriers for axon regeneration in the adult CNS. Curr Opin Neurobiol *20*, 510–518. https://doi.org/10.1016/j.conb.2010.03.013.
2. Venkatesh, I., and Blackmore, M.G. (2017). Selecting optimal combinations of transcription factors to promote axon regeneration: Why mechanisms matter. Neuroscience Letters *652*, 64–73. https://doi.org/10.1016/j.neulet.2016.12.032.
3. Mahar, M., and Cavalli, V. (2018). Intrinsic mechanisms of neuronal axon regeneration. Nat Rev Neurosci *19*, 323–337. https://doi.org/10.1038/s41583-018-0001-8.
4. Wang, Z., Mehra, V., Simpson, M.T., Maunze, B., Chakraborty, A., Holan, L., Eastwood, E., Blackmore, M.G., and Venkatesh, I. (2018). KLF6 and STAT3 co-occupy regulatory DNA and functionally synergize to promote axon growth in CNS neurons. Sci Rep *8*, 12565. https://doi.org/10.1038/s41598-018-31101-5.
5. Blackmore, M.G. (2012). Molecular control of axon growth: insights from comparative gene profiling and high-throughput screening. Int Rev Neurobiol *105*, 39–70. https://doi.org/10.1016/B978-0-12-398309-1.00004-4.
6. Wang, Z., Kumaran, M., Batsel, E., Testor-Cabrera, S., Beine, Z., Alvarez Ribelles, A., Tsoulfas, P., Venkatesh, I., and Blackmore, M.G. (2025). Single-nuclei sequencing reveals a robust corticospinal response to nearby axotomy but overall insensitivity to spinal injury. J. Neurosci., e1508242024. https://doi.org/10.1523/JNEUROSCI.1508-24.2024.
7. Moore, D.L., Blackmore, M.G., Hu, Y., Kaestner, K.H., Bixby, J.L., Lemmon, V.P., and Goldberg, J.L. (2009). KLF family members regulate intrinsic axon regeneration ability. Science *326*, 298–301. https://doi.org/10.1126/science.1175737.
8. Jacobi, A., Tran, N.M., Yan, W., Benhar, I., Tian, F., Schaffer, R., He, Z., and Sanes, J.R. (2022). Overlapping transcriptional programs promote survival and axonal regeneration of injured retinal ganglion cells. Neuron *110*, 2625-2645.e7. https://doi.org/10.1016/j.neuron.2022.06.002.
9. Sun, F., Park, K.K., Belin, S., Wang, D., Lu, T., Chen, G., Zhang, K., Yeung, C., Feng, G., Yankner, B.A., et al. (2011). Sustained axon regeneration induced by co-deletion of PTEN and SOCS3. Nature *480*, 372–375. https://doi.org/10.1038/nature10594.
10. Shin, J.E., Cho, Y., Beirowski, B., Milbrandt, J., Cavalli, V., and DiAntonio, A. (2012). Dual Leucine Zipper Kinase Is Required for Retrograde Injury Signaling and Axonal Regeneration. Neuron *74*, 1015–1022. https://doi.org/10.1016/j.neuron.2012.04.028.
11. Yiu, G., and He, Z. (2006). Glial inhibition of CNS axon regeneration. Nat Rev Neurosci *7*, 617–627. https://doi.org/10.1038/nrn1956.

12. Fawcett, J.W., and Asher, Richard.A. (1999). The glial scar and central nervous system repair. Brain Research Bulletin *49*, 377–391. https://doi.org/10.1016/S0361-9230(99)00072-6.
13. Venkatesh, I., Mehra, V., Wang, Z., Califf, B., and Blackmore, M.G. (2018). Developmental Chromatin Restriction of Pro-Growth Gene Networks Acts as an Epigenetic Barrier to Axon Regeneration in Cortical Neurons. Dev Neurobiol *78*, 960–977. https://doi.org/10.1002/dneu.22605.
14. Venkatesh, I., Simpson, M.T., Coley, D.M., and Blackmore, M.G. (2016). Epigenetic profiling reveals a developmental decrease in promoter accessibility during cortical maturation *in vivo*. Neuroepigenetics *8*, 19–26. https://doi.org/10.1016/j.nepig.2016.10.002.
15. Blackmore, M.G., Moore, D.L., Smith, R.P., Goldberg, J.L., Bixby, J.L., and Lemmon, V.P. (2010). High content screening of cortical neurons identifies novel regulators of axon growth. Molecular and Cellular Neuroscience *44*, 43–54. https://doi.org/10.1016/j.mcn.2010.02.002.
16. Seijffers, R., Mills, C.D., and Woolf, C.J. (2007). ATF3 Increases the Intrinsic Growth State of DRG Neurons to Enhance Peripheral Nerve Regeneration. J. Neurosci. *27*, 7911–7920. https://doi.org/10.1523/JNEUROSCI.5313-06.2007.
17. Simpson, M.T., Venkatesh, I., Callif, B.L., Thiel, L.K., Coley, D.M., Winsor, K.N., Wang, Z., Kramer, A.A., Lerch, J.K., and Blackmore, M.G. (2015). The tumor suppressor HHEX inhibits axon growth when prematurely expressed in developing central nervous system neurons. Molecular and Cellular Neuroscience *68*, 272–283. https://doi.org/10.1016/j.mcn.2015.08.008.
18. Williams, R.R., Venkatesh, I., Pearse, D.D., Udvadia, A.J., and Bunge, M.B. (2015). MASH1/Ascl1a Leads to GAP43 Expression and Axon Regeneration in the Adult CNS. PLoS ONE *10*, e0118918. https://doi.org/10.1371/journal.pone.0118918.
19. Dhara, S.P., Rau, A., Flister, M.J., Recka, N.M., Laiosa, M.D., Auer, P.L., and Udvadia, A.J. (2019). Cellular reprogramming for successful CNS axon regeneration is driven by a temporally changing cast of transcription factors. Sci Rep *9*, 14198. https://doi.org/10.1038/s41598-019-50485-6.
20. Venkatesh, I., Mehra, V., Wang, Z., Simpson, M.T., Eastwood, E., Chakraborty, A., Beine, Z., Gross, D., Cabahug, M., Olson, G., et al. (2021). Co-occupancy identifies transcription factor co-operation for axon growth. Nat Commun *12*, 2555. https://doi.org/10.1038/s41467-021-22828-3.

21. Chandran, V., Coppola, G., Nawabi, H., Omura, T., Versano, R., Huebner, E.A., Zhang, A., Costigan, M., Yekkirala, A., Barrett, L., et al. (2016). A Systems-Level Analysis of the Peripheral Nerve Intrinsic Axonal Growth Program. Neuron *89*, 956–970. https://doi.org/10.1016/j.neuron.2016.01.034.
22. Avraham, O., Le, J., Leahy, K., Li, T., Zhao, G., and Cavalli, V. (2022). Analysis of neuronal injury transcriptional response identifies CTCF and YY1 as co-operating factors regulating axon regeneration. Front Mol Neurosci *15*, 967472. https://doi.org/10.3389/fnmol.2022.967472.
23. Bareyre, F.M., Garzorz, N., Lang, C., Misgeld, T., Büning, H., and Kerschensteiner, M. (2011). In vivo imaging reveals a phase-specific role of STAT3 during central and peripheral nervous system axon regeneration. Proc. Natl. Acad. Sci. U.S.A. *108*, 6282–6287. https://doi.org/10.1073/pnas.1015239108.
24. Raivich, G., Bohatschek, M., Da Costa, C., Iwata, O., Galiano, M., Hristova, M., Nateri, A.S., Makwana, M., Riera-Sans, L., Wolfer, D.P., et al. (2004). The AP-1 Transcription Factor c-Jun Is Required for Efficient Axonal Regeneration. Neuron *43*, 57–67. https://doi.org/10.1016/j.neuron.2004.06.005.
25. Mehta, S.T., Luo, X., Park, K.K., Bixby, J.L., and Lemmon, V.P. (2016). Hyperactivated Stat3 boosts axon regeneration in the CNS. Exp Neurol *280*, 115–120. https://doi.org/10.1016/j.expneurol.2016.03.004.
26. Li, S., Xue, C., Yuan, Y., Zhang, R., Wang, Y., Wang, Y., Yu, B., Liu, J., Ding, F., Yang, Y., et al. (2015). The transcriptional landscape of dorsal root ganglia after sciatic nerve transection. Sci Rep *5*, 16888. https://doi.org/10.1038/srep16888.
27. Ephraim F. Trakhtenberg, Ephraim F. Trakhtenberg, Jeffrey L. Goldberg, and Jeffrey L. Goldberg (2012). Epigenetic regulation of axon and dendrite growth. Frontiers in Molecular Neuroscience. https://doi.org/10.3389/fnmol.2012.00024.
28. Finelli, M.J., Wong, J.K., and Zou, H. (2013). Epigenetic Regulation of Sensory Axon Regeneration after Spinal Cord Injury. J. Neurosci. *33*, 19664–19676. https://doi.org/10.1523/JNEUROSCI.0589-13.2013.
29. VandenBosch, L.S., and Reh, T.A. (2020). Epigenetics in neuronal regeneration. Seminars in Cell & Developmental Biology *97*, 63–73. https://doi.org/10.1016/j.semcdb.2019.04.001.
30. Puttagunta, R., Tedeschi, A., Sória, M.G., Hervera, A., Lindner, R., Rathore, K.I., Gaub, P., Joshi, Y., Nguyen, T., Schmandke, A., et al. (2014). PCAF-dependent epigenetic

changes promote axonal regeneration in the central nervous system. Nat Commun *5*, 3527. https://doi.org/10.1038/ncomms4527.

31. Gaub, P., Tedeschi, A., Puttagunta, R., Nguyen, T., Schmandke, A., and Di Giovanni, S. (2010). HDAC inhibition promotes neuronal outgrowth and counteracts growth cone collapse through CBP/p300 and P/CAF-dependent p53 acetylation. Cell Death Differ *17*, 1392–1408. https://doi.org/10.1038/cdd.2009.216.
32. Gaub, P., Joshi, Y., Wuttke, A., Naumann, U., Schnichels, S., Heiduschka, P., and Di Giovanni, S. (2011). The histone acetyltransferase p300 promotes intrinsic axonal regeneration. Brain *134*, 2134–2148. https://doi.org/10.1093/brain/awr142.
33. Tedeschi, A., Nguyen, T., Puttagunta, R., Gaub, P., and Di Giovanni, S. (2009). A p53-CBP/p300 transcription module is required for GAP-43 expression, axon outgrowth, and regeneration. Cell Death Differ *16*, 543–554. https://doi.org/10.1038/cdd.2008.175.
34. Weng, Y.-L., An, R., Cassin, J., Joseph, J., Mi, R., Wang, C., Zhong, C., Jin, S.-G., Pfeifer, G.P., Bellacosa, A., et al. (2017). An Intrinsic Epigenetic Barrier for Functional Axon Regeneration. Neuron *94*, 337-346.e6. https://doi.org/10.1016/j.neuron.2017.03.034.
35. Ilaria Palmisano, Ilaria Palmisano, Matt C. Danzi, Matt C. Danzi, Thomas E. Hutson, Thomas H. Hutson, Luming Zhou, Luming Zhou, Eilidh McLachlan, Eilidh McLachlan, et al. (2019). Epigenomic signatures underpin the axonal regenerative ability of dorsal root ganglia sensory neurons. Nature Neuroscience. https://doi.org/10.1038/s41593-019-0490-4.
36. Palmisano, I., Liu, T., Gao, W., Zhou, L., Merkenschlager, M., Mueller, F., Chadwick, J., Toscano Rivalta, R., Kong, G., King, J.W.D., et al. (2024). Three-dimensional chromatin mapping of sensory neurons reveals that promoter–enhancer looping is required for axonal regeneration. Proc. Natl. Acad. Sci. U.S.A. *121*, e2402518121. https://doi.org/10.1073/pnas.2402518121.
37. The ENCODE Project Consortium, Abascal, F., Acosta, R., Addleman, N.J., Adrian, J., Afzal, V., Ai, R., Aken, B., Akiyama, J.A., Jammal, O.A., et al. (2020). Expanded encyclopaedias of DNA elements in the human and mouse genomes. Nature *583*, 699–710. https://doi.org/10.1038/s41586-020-2493-4.
38. Highly interacting regions of the human genome are enriched with enhancers and bound by DNA repair proteins | Scientific Reports https://www.nature.com/articles/s41598-019-40770-9.
39. Zhao, Y., Vartak, S.V., Conte, A., Wang, X., Garcia, D.A., Stevens, E., Jung, S.K., Kieffer-Kwon, K.-R., Vian, L., Stodola, T., et al. (2022). “Stripe” transcription factors provide

accessibility to co-binding partners in mammalian genomes. Molecular Cell *82*, 3398-3411.e11. https://doi.org/10.1016/j.molcel.2022.06.029.

40. Ma, H., Ow, J.R., Tan, B.C.P., Goh, Z., Feng, B., Loh, Y.H., Fedele, M., Li, H., and Wu, Q. (2014). The dosage of Patz1 modulates reprogramming process. Sci Rep *4*, 7519. https://doi.org/10.1038/srep07519.
41. Mancinelli, S., Vitiello, M., Donnini, M., Mantile, F., Palma, G., Luciano, A., Arra, C., Cerchia, L., Liguori, G.L., and Fedele, M. (2021). The Transcription Regulator Patz1 Is Essential for Neural Stem Cell Maintenance and Proliferation. Front. Cell Dev. Biol. *9*. https://doi.org/10.3389/fcell.2021.657149.
42. Ow, J.R., Ma, H., Jean, A., Goh, Z., Lee, Y.H., Chong, Y.M., Soong, R., Fu, X.-Y., Yang, H., and Wu, Q. (2014). Patz1 Regulates Embryonic Stem Cell Identity. Stem Cells and Development *23*, 1062–1073. https://doi.org/10.1089/scd.2013.0430.
43. Valentino, T., Palmieri, D., Vitiello, M., Simeone, A., Palma, G., Arra, C., Chieffi, P., Chiariotti, L., Fusco, A., and Fedele, M. (2013). Embryonic defects and growth alteration in mice with homozygous disruption of the *Patz1* gene. J. Cell. Physiol. *228*, 646–653. https://doi.org/10.1002/jcp.24174.
44. Norsworthy, M.W., Bei, F., Kawaguchi, R., Wang, Q., Tran, N.M., Li, Y., Brommer, B., Zhang, Y., Wang, C., Sanes, J.R., et al. (2017). Sox11 Expression Promotes Regeneration of Some Retinal Ganglion Cell Types but Kills Others. Neuron *94*, 1112-1120.e4. https://doi.org/10.1016/j.neuron.2017.05.035.
45. Laub, F., Aldabe, R., Friedrich, V., Ohnishi, S., Yoshida, T., and Ramirez, F. (2001). Developmental Expression of Mouse Krüppel-like Transcription Factor KLF7 Suggests a Potential Role in Neurogenesis. Developmental Biology *233*, 305–318. https://doi.org/10.1006/dbio.2001.0243.
46. Kramer, A.A., Olson, G.M., Chakraborty, A., and Blackmore, M.G. (2021). Promotion of corticospinal tract growth by KLF6 requires an injury stimulus and occurs within four weeks of treatment. Experimental Neurology *339*, 113644. https://doi.org/10.1016/j.expneurol.2021.113644.
47. Starkey, M.L., Barritt, A.W., Yip, P.K., Davies, M., Hamers, F.P.T., McMahon, S.B., and Bradbury, E.J. (2005). Assessing behavioural function following a pyramidotomy lesion of the corticospinal tract in adult mice. Experimental Neurology *195*, 524–539. https://doi.org/10.1016/j.expneurol.2005.06.017.
48. Kumaran, M., Narayan, P.A., Sahu, Y., Banerjee, S., Menon, A.S., Soni, S., and Venkatesh, I. (2025). Deep Neurite Analysis Tool (DeNAT): A machine-learning framework for

precise automated neurite outgrowth measurement. Preprint at bioRxiv, https://doi.org/10.1101/2025.09.18.676567 https://doi.org/10.1101/2025.09.18.676567.

49. NIH Image to ImageJ: 25 years of image analysis | Nature Methods https://www.nature.com/articles/nmeth.2089.
50. Satpathy, A.T., Granja, J.M., Yost, K.E., Qi, Y., Meschi, F., McDermott, G.P., Olsen, B.N., Mumbach, M.R., Pierce, S.E., Corces, M.R., et al. (2019). Massively parallel single-cell chromatin landscapes of human immune cell development and intratumoral T cell exhaustion. Nat Biotechnol *37*, 925–936. https://doi.org/10.1038/s41587-019-0206-z.
51. Granja, J.M., Corces, M.R., Pierce, S.E., Bagdatli, S.T., Choudhry, H., Chang, H.Y., and Greenleaf, W.J. (2021). ArchR is a scalable software package for integrative single-cell chromatin accessibility analysis. Nat Genet *53*, 403–411. https://doi.org/10.1038/s41588-021-00790-6.
52. Chen, S., Zhou, Y., Chen, Y., and Gu, J. (2018). fastp: an ultra-fast all-in-one FASTQ preprocessor. Bioinformatics *34*, i884–i890. https://doi.org/10.1093/bioinformatics/bty560.
53. Dobin, A., Davis, C.A., Schlesinger, F., Drenkow, J., Zaleski, C., Jha, S., Batut, P., Chaisson, M., and Gingeras, T.R. (2013). STAR: ultrafast universal RNA-seq aligner. Bioinformatics *29*, 15–21. https://doi.org/10.1093/bioinformatics/bts635.
54. Li, H., Handsaker, B., Wysoker, A., Fennell, T., Ruan, J., Homer, N., Marth, G., Abecasis, G., Durbin, R., and 1000 Genome Project Data Processing Subgroup (2009). The Sequence Alignment/Map format and SAMtools. Bioinformatics *25*, 2078–2079. https://doi.org/10.1093/bioinformatics/btp352.
55. Bentsen, M., Goymann, P., Schultheis, H., Klee, K., Petrova, A., Wiegandt, R., Fust, A., Preussner, J., Kuenne, C., Braun, T., et al. (2020). ATAC-seq footprinting unravels kinetics of transcription factor binding during zygotic genome activation. Nat Commun *11*, 4267. https://doi.org/10.1038/s41467-020-18035-1.
56. Raney, B.J., Barber, G.P., Benet-Pagès, A., Casper, J., Clawson, H., Cline, M.S., Diekhans, M., Fischer, C., Navarro Gonzalez, J., Hickey, G., et al. (2024). The UCSC Genome Browser database: 2024 update. Nucleic Acids Research *52*, D1082–D1088. https://doi.org/10.1093/nar/gkad987.
57. Bentsen, M., Heger, V., Schultheis, H., Kuenne, C., and Looso, M. (2022). TF-COMB – Discovering grammar of transcription factor binding sites. Computational and Structural Biotechnology Journal *20*, 4040–4051. https://doi.org/10.1016/j.csbj.2022.07.025.

58. Fast and accurate short read alignment with Burrows–Wheeler transform | Bioinformatics | Oxford Academic https://academic.oup.com/bioinformatics/article/25/14/1754/225615.
59. Zhang, Y., Liu, T., Meyer, C.A., Eeckhoute, J., Johnson, D.S., Bernstein, B.E., Nusbaum, C., Myers, R.M., Brown, M., Li, W., et al. (2008). Model-based Analysis of ChIP-Seq (MACS). Genome Biol *9*, R137. https://doi.org/10.1186/gb-2008-9-9-r137.
60. Yu, G., Wang, L.-G., and He, Q.-Y. (2015). ChIPseeker: an R/Bioconductor package for ChIP peak annotation, comparison and visualization. Bioinformatics *31*, 2382–2383. https://doi.org/10.1093/bioinformatics/btv145.
61. Zheng, G.X.Y., Terry, J.M., Belgrader, P., Ryvkin, P., Bent, Z.W., Wilson, R., Ziraldo, S.B., Wheeler, T.D., McDermott, G.P., Zhu, J., et al. (2017). Massively parallel digital transcriptional profiling of single cells. Nat Commun *8*, 14049. https://doi.org/10.1038/ncomms14049.
62. Butler, A., Hoffman, P., Smibert, P., Papalexi, E., and Satija, R. (2018). Integrating single-cell transcriptomic data across different conditions, technologies, and species. Nat Biotechnol *36*, 411–420. https://doi.org/10.1038/nbt.4096.
63. Ouyang, J.F., Kamaraj, U.S., Cao, E.Y., and Rackham, O.J.L. (2021). ShinyCell: simple and sharable visualization of single-cell gene expression data. Bioinformatics *37*, 3374–3376. https://doi.org/10.1093/bioinformatics/btab209.
64. Brown, J., Pirrung, M., and McCue, L.A. (2017). FQC Dashboard: integrates FastQC results into a web-based, interactive, and extensible FASTQ quality control tool. Bioinformatics *33*, 3137–3139. https://doi.org/10.1093/bioinformatics/btx373.
65. Langmead, B., and Salzberg, S.L. (2012). Fast gapped-read alignment with Bowtie 2. Nat Methods *9*, 357–359. https://doi.org/10.1038/nmeth.1923.
66. Durand, N.C., Robinson, J.T., Shamim, M.S., Machol, I., Mesirov, J.P., Lander, E.S., and Aiden, E.L. (2016). Juicebox Provides a Visualization System for Hi-C Contact Maps with Unlimited Zoom. Cell Syst *3*, 99–101. https://doi.org/10.1016/j.cels.2015.07.012.
67. Heinz, S., Benner, C., Spann, N., Bertolino, E., Lin, Y.C., Laslo, P., Cheng, J.X., Murre, C., Singh, H., and Glass, C.K. (2010). Simple combinations of lineage-determining transcription factors prime cis-regulatory elements required for macrophage and B cell identities. Mol Cell *38*, 576–589. https://doi.org/10.1016/j.molcel.2010.05.004.
68. Robinson, M.D., McCarthy, D.J., and Smyth, G.K. (2010). edgeR : a Bioconductor package for differential expression analysis of digital gene expression data. Bioinformatics *26*, 139–140. https://doi.org/10.1093/bioinformatics/btp616.